IEEE Access
Multidisciplinary | Rapid Review | Open Access Journal

Received 10 August 2022, accepted 7 September 2022, date of publication 12 September 2022,
date of current version 26 September 2022.

Digital Object Identifier 10.1109/ACCESS.2022.3206358

RESEARCH ARTICLE

Modeling of a Negative Refractive Index Metamaterial Unit-Cell and Array for Aircraft Surveillance Applications

M. PALLAVI[1,2], (Member, IEEE), PRAMOD KUMAR[1], (Senior Member, IEEE), TANWEER ALI[1], (Senior Member, IEEE), AND SATISH B. SHENOY[2,3], (Member, IEEE)

[1]Department of Electronics and Communication Engineering, Manipal Institute of Technology, Manipal Academy of Higher Education, Manipal 576104, India
[2]Centre of Excellence in Avionics and Navigation, Manipal Academy of Higher Education, Manipal 576104, India
[3]Department of Aeronautical and Automobile Engineering, Manipal Institute of Technology, Manipal Academy of Higher Education, Manipal 576104, India

Corresponding author: Pramod Kumar (p.kumar@manipal.edu)

ABSTRACT In this paper, a unique negative refractive index-metamaterial (NRI-MTM) structure is proposed for traffic alert and collision avoidance system (TCAS) for aircraft application. The NRI-MTM unit-cell structure is a combination of square and circular split ring structures. The proposed square and circular split ring metamaterial (SCM) is designed on the top of a 1.6 mm thick FR-4 substrate, with a single circular split ring on the bottom of the substrate. The total dimension of the SCM unit-cell is $23 \times 23\text{mm}^2$ ($0.08\lambda \times 0.08\lambda$), resonating at 1.06 GHz. This unit-cell is further used to create a 5×4 array structure with a dimension of $130 \times 111\text{mm}^2$ ($0.46\lambda \times 0.4\lambda$). A High-Frequency Structure Simulator (HFSS) is used to assess the electromagnetic properties of the proposed structures. Furthermore, in order to analyse the double negative (DNG) behaviour of the designed SCM structure, the unit-cell is rotated from 0 to 360 degrees with a step of 60 degrees along the azimuthal plane. On doing so, it is observed that, the proposed SCM structures, including unit-cell and array structures, exhibit DNG and NRI properties over the frequency band of 0.5 to 1.2 GHz, thus making it optimum for aircraft surveillance application. The SCM unit-cell and 5×4 SCM array structure were fabricated, and the measured results are in well agreement with the simulated results. Further, the array structure is used as a superstrate on the patch antenna to analyze the impact of the MTM on the antenna performance. In comparison to the antenna without the MTM structure, the 5×4 SCM array loaded antenna has a gain improvement of 2.8dB and a bandwidth enhancement of 31.5MHz.

INDEX TERMS Metamaterial, metamaterial slab, double negative, negative-refractive index, permittivity, permeability.

I. INTRODUCTION

The naturally available materials such as metals, ceramics, polymers, and glasses are processed in many different ways to develop new materials or breakthroughs in order to upgrade present technology to its utmost level. Natural materials have significant limitations in terms of generating exotic features for different applications. The synthetic material having an overall dimension less than the operating wavelength and exhibits exotic properties like negative permittivity (ε), negative permeability (μ), and negative refractive index (n) is well known as metamaterial (MTM).

The conception of MTM inspired many researchers to construct a distinctive contribution in the research field. The exceptional behavior of MTM is not determined by the base materials; rather, its properties are influenced by the precise shape, size, geometry, and orientations. From a pragmatic perspective, MTM offers some special electromagnetic (EM) features that are not typically available in conventional materials [1].

In contrast to natural materials, the MTM interacts with both light and sound waves in unanticipated patterns.

The associate editor coordinating the review of this manuscript and approving it for publication was Guido Valerio.

The MTM has the potential to control the propagation of light inside waveguides and in free space [2]. Therefore, the ability to influence the propagation of EM waves and the outstanding features of MTM made it appropriate for various applications such as antennas, satellite communication, optical filters, invisibility cloaking, shielding properties, biosensors, sensor detection, signal multiplexing, holography, data processing, and battlefield communication [3], [4], [5], [6], [7], [8], [9], [10], [11], [12], [13].

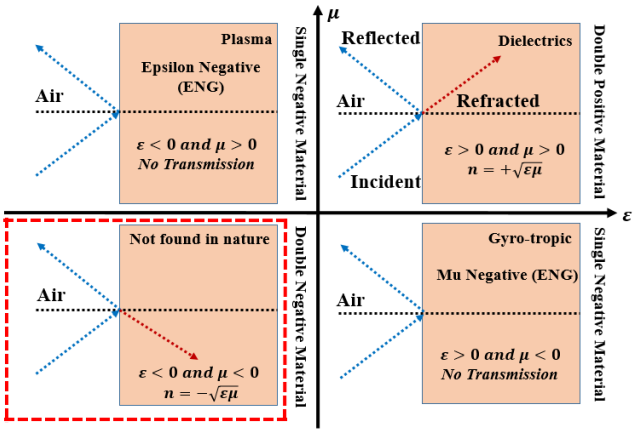

FIGURE 1. Classification of metamaterial.

The MTMs are classified based on their EM properties as shown in Figure 1 [14]. The material is classified as Double Positive (DPS) if its 'ε' and 'μ' values are positive. All naturally available materials are DPS, and they will fall under quadrant I (QI). If one of the material parameters, either 'ε' or 'μ', is negative, the material falls into quadrant II or IV and is referred to as a Single Negative (SNG) material [15]. Double Negative (DNG) material, which belongs to quadrant III, is the most versatile MTM class type. In this material, both 'ε' and 'μ' values become negative. The MTM with DNG will exhibit many exceptional properties, and its behavior will be completely different from the primitive laws [16]. Since the refractive index (n) in DNG is always less than zero, the inclination of the phase and group velocities is in the opposite direction, reversing the direction of wave propagation with reference to the energy flow direction [17]. These DNG materials are used for various applications, which include antenna design. DNG materials have a significant impact on antenna parameters, specifically gain, bandwidth, and polarization.

The concept of MTM with negative 'ε' and negative 'μ' was first evinced by the Russian scientist V.G. Veselago in 1968 [18]. The author used a lossless MTM to theoretically explain the propagation of EM waves and their extraordinary properties such as negative refraction, reverse Doppler effect, Cerenkov radiation, and negative group speed, that are not discovered in naturally available materials. Veselego's theory remained idle for almost 29 years till Prof J.B Pendry introduced the combination of Thin-Wire (TW) and the Split Ring Resonator (SRR) structure in the year 1996, where the SRR structure exhibits the negative 'μ' [19] and the TW structure exhibits the negative 'ε' [20]. Later, D.R Smith et al proposed the new MTM structure with negative 'ε' and negative 'μ' in the year 2000, and it was experimentally tested to obtain its exceptional properties [21]. The MTM slab having two dimensional (2D) array of uniformly reiterated unit-cells of SRR and copper strips are experimentally validated for negative refraction by Shelby et al in 2001 [22].

A novel MTM unit-cell for satellite applications was proposed in [23]. The proposed MTM structure was developed on a 1.6mm thick FR-4 dielectric substrate with an overall dimension of 30 $\times$ 30mm^2. For the parametric analysis and comparative study, different substrate materials such as lossy Polymide, Aluminum Nitride, and Rogers RT 6010 were utilized. The combination of SRR and a capacitive loaded strip (CLS) MTM was presented for L and S frequency band operation in [24]. The primary objective of the proposed MTM is to improve the gain of the patch antenna. The inclusion of CLS has added additional capacitance to the structure, resulting in a lower stop-band.

A novel three different triangular-shaped SRR with CLS was proposed in [25]. The two coupled triangular SRR was combined with CLS to generate the DNG character for the frequency spectrum ranging from 2.5GHz to 6GHz. All three triangle MTM configurations were simulated on 2 separate substrates, FR-4 and RT/Duroid 5880, in order to analyze and compare the parameters. A novel MTM unit-cell comprising a circular-shaped single-loop resonator (SLR) and a pair of short capacitor-loaded strips was proposed in [26]. The proposed MTM structure was developed on a 0.8mm thick Rogers 6006 substrate with an overall dimension of 15 $\times$ 15 mm^2. This novel structure exhibits DNG characteristics in the frequency range of 0.5GHz to 3GHz, making it appropriate for L and S-band applications.

A circular, square, triangular, and hybrid single-loop resonator (SLR) MTMs was proposed in [27]. All four MTM structures were simulated on a 1mm thick Rogers 3003 substrate. Initially, circular, square, and triangular MTMs were developed, with all of the designs exhibiting multi-band operation with a relatively narrow bandwidth. To improve bandwidth and expand the number of frequency bands, a hybrid SLR was developed by combining square and triangle-shaped resonators. The new hybrid SLR design has increased the number of frequency bands from three to four, considerably improving bandwidth. The proposed MTM structure is suitable for S and L bands with a frequency ranging from 2.5 GHz to 5.5 GHz. Similarly, for L and S frequency band applications, a significant number of DNG MTM structures have been proposed, including S-shape [28], Ω -shape [29], broadside-coupled (BC) and modified BC [30], open-loop single square [31], and H-shape [32].

In [33], a quad-element patch antenna positioned in circular fashion was proposed for aircraft surveillance application. A traditional MTM with a combination of square SRR and TW structure is designed on a flexible Teflon dielectric substrate to maximize the gain of the antenna. The MTM unit-cell has an overall dimension of 30 $\times$ 30mm^2 and an

effective medium ratio of 9.4. In this study, 8 layers of 3×4 and 8 layers of 2×4 MTM slab were deployed around all four directions of the antenna to achieve an 8.2 dB gain enhancement (Conventional antenna gain is 6.9dB).

In surveillance applications, a high gain antenna is essential for achieving a focused, narrow beam width and more accurate radio transmission targeting. In addition to high gain, wider bandwidth is also important to maximize channel capacity, extend surveillance over a larger area, and improve airspace efficiency. Hence, a compact, simple, low-profile, high gain, and broad bandwidth MTM loaded patch antenna is needed for this application.

In this research, a unique combination of square and circular split ring resonator (SCSRR) with open stubs are used to create a novel NRI-MTM for enhancing the bandwidth and gain of the Traffic alert and collision avoidance system (TCAS) antenna. The coupled SCSRR design on top of the substrate generates the negative 'μ' at the 1.06 GHz resonant frequency. The TW structure was adopted in many prior studies to generate negative 'ε', however, in this work, the TW structure is substituted by a circular SRR of finite dimension to accomplish negative 'ε' characteristics. The proposed NRI-MTM array is utilized as a superstrate to examine the impact on antenna performance, particularly antenna gain and bandwidth.

The article is organized as follows: Section II details the theoretical analysis of the proposed SCM unit-cell, Section III describes design and the characteristic analysis of the SCM unit-cell, Section IV discusses the results and discussion of the proposed SCM structures, and Section V concludes the work with potential future directions.

II. THEORETICAL ANALYSIS OF SCM UNIT-CELL

The SCM is a hybrid MTM structure. The standard expressions are used to construct each square and circular SRRs. Initially, the theoretical procedure for constructing the outer square SRR with a single gap is described. Later, the procedure adopted to construct the circular SRRs is discussed.

The structure and cross-section of the single outer square SRR are depicted in Figure 2(a). At the resonating frequency, the square SRR will be represented as a parallel LC circuit as shown in Figure 2(b).

The overall capacitance (C_1) is the summation of the surface capacitance (C_{Surf}) and the gap capacitance (C_{gap}). When a square SRR structure is exposed to a magnetic field imposed across the y-axis, an electromotive force (EMF) is induced across the square SRR, making the structure to function like an LC network with a resonating frequency (f_{01}) expressed as [34]

$$f_{01} = \frac{1}{2\pi\sqrt{L_1 C_1}} \tag{1}$$

where, L_1 is the inductance which represents the total length of the square ring, and C_1 is the total capacitance.

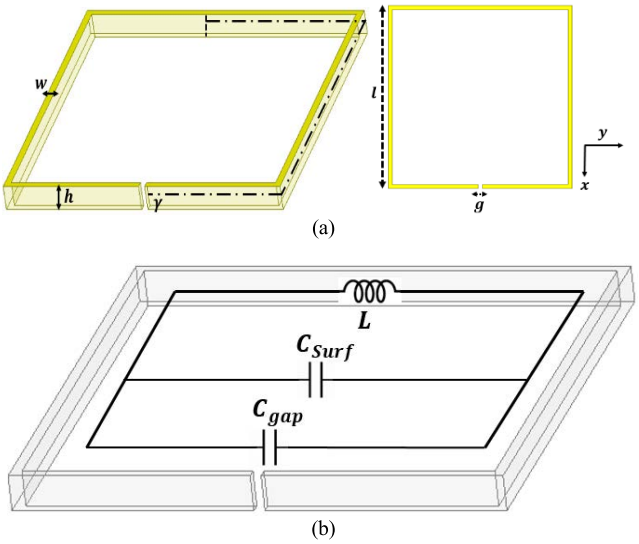

FIGURE 2. (a) The 3D structure and cross-section of outer square SRR (b) Equivalent LC circuit of outer square SRR. Classification of metamaterial.

The inductance L_1 and capacitance C_1 are expressed as

$$L_1 = \mu_0 a_m \left(ln\frac{8a_m}{h+w} - 0.5 \right) \tag{2}$$

where a_m denotes the mean length of the square ring, $a_m = a + \frac{w}{2}$, h is height, and w is thickness.

The total capacitance (C_1), which is the combination of gap and the surface capacitance is given by

$$\frac{1}{C_1} = \frac{1}{C_{gap}} + \frac{1}{C_{Surf}} \tag{3}$$

where the expressions for C_{gap} and C_{Surf} is given by

$$C_{gap} = \varepsilon_0 \left(\frac{wh}{g} + \frac{2\pi h}{ln\left(\frac{2.4h}{w}\right)} \right) \tag{4}$$

$$C_{Surf} = \frac{2\varepsilon_0 h}{\pi} ln\frac{4a}{g} \tag{5}$$

where g denotes split gap width of square SRR.

By substituting the values $\mu_0 = 4\pi \times 10^{-7}\text{N/A}^2$, $a = 11.25mm$, $h = 1.6mm$, $w = 1mm$, $g = 0.5mm$, and $\varepsilon_0 = 8.85 \times 10^{-12}\text{F/m}$, an inductance ($L_1$) value of 71.32 nH and capacitance (C_1) value of 685.97 pF were theoretically recorded for the outer square SRR structure. Hence, the f_{01} for the outermost ring without coupling effect is 0.72 GHz.

To find the f_{01} with coupling effect, the separation distance between outermost SRR and the consecutive SRR needs to be included in the calculation. In our design, the distance between two SRR is 5.6mm, hence, the f_{01} for the outermost ring is 1.61 GHz which is close to the simulated value (1.7GHz).

The structure and cross-section of a single split inner circular SRR is depicted in Figure 3(a), whereas Figure 3(b) illustrates its equivalent LC circuit. For the circular ring

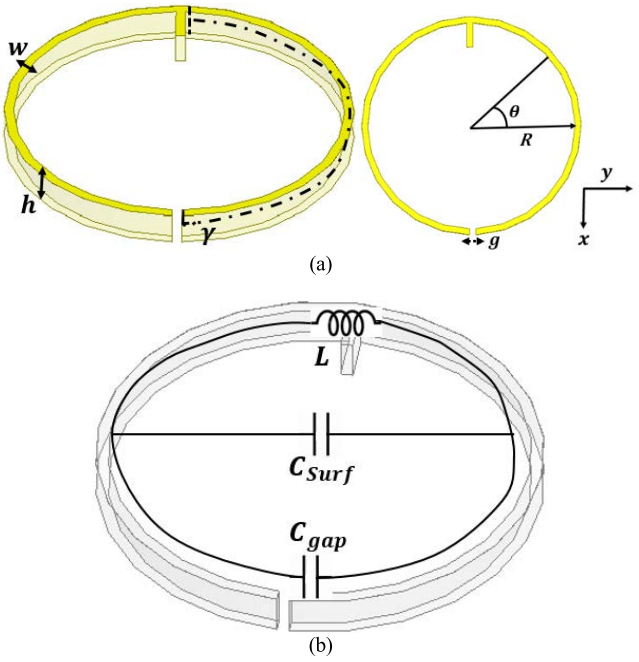

FIGURE 3. (a) The 3D structure and cross-section of inner circular SRR (b) Equivalent LC circuit of inner circular SRR.

structure, the resonating frequency, f_{02} is given by [35], [36]

$$f_{02} = \frac{1}{2\pi\sqrt{L_2 C_2}} \tag{6}$$

where, L_2 is the inductance which represents the diameter of the circular ring, and C_2 is the total capacitance.

The inductance (L_2) and capacitance (C_2) can be expressed as

$$L_2 = \mu_0 R_m \left(ln\frac{8R_m}{h+w} - 0.5 \right) \tag{7}$$

where R_m is the circular ring mean radius, $R_m = R + \frac{w}{2}$.

$$C_{gap} = \varepsilon_0 \left(\frac{wh}{g} + \frac{2\pi h}{ln\left(\frac{2.4h}{w}\right)} \right) \tag{8}$$

$$C_{Surf} = \int_{\theta_g}^{\pi} \frac{\sigma R d\theta}{V} = \varepsilon_0 h \int_{\theta_g}^{\pi} \frac{cot\left(\frac{\theta}{2}\right)}{\pi - \theta} d\theta \approx \frac{2\varepsilon_0 h}{\pi} ln\frac{4R}{g} \tag{9}$$

The following expressions are used to calculate the σ and V,

$$\sigma = \frac{\varepsilon_0 V_0}{2\pi R} cot\frac{\theta}{2}; \quad V = \frac{C_2}{\pi}(\pi - \theta) \tag{10}$$

where θ is the angle depicted in Figure 3(a), and V_0 denotes the applied voltage across the gap.

The total capacitance (C_2) is given by,

$$\frac{1}{C_2} = \frac{1}{C_{gap}} + \frac{1}{C_{Surf}} \tag{11}$$

By substituting the values $\mu_0 = 4\pi \times 10^{-7}$N/A^2, $R = 9mm$, $h = 1.6mm$, $w = 0.5mm$, $g = 0.5mm$, and $\varepsilon_0 = 8.85 \times 10^{-12}$F/m, an inductance ($L_2$) value of 45.4297 nH and capacitance (C_2) value of 473.70 pF were theoretically recorded. Hence, the f_{02} for the outer circular SRR structure is 1.08 GHz. Since, this is the innermost SRR without any following SRR structure, the resonating frequency remains unchanged for with and without coupling.

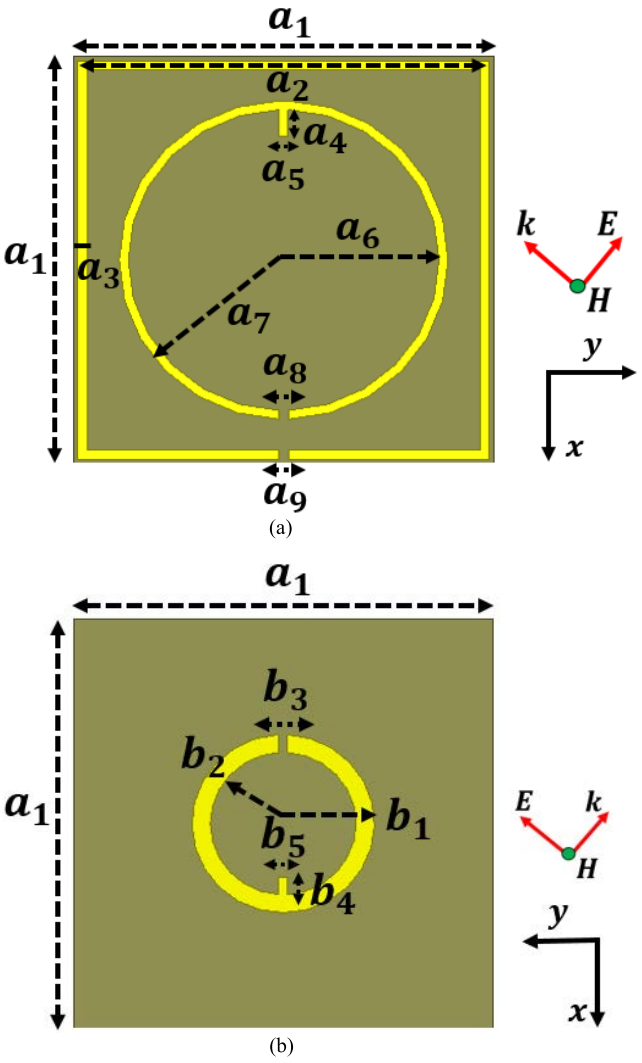

FIGURE 4. SCM design: (a) top-view and (b) bottom-view.

The same procedure was followed to calculate the ground circular SRR structure. By substituting the values $\mu_0 = 4\pi \times 10^{-7}$N/A^2, $R = 5mm$, $h = 1.6mm$, $w = 1mm$, $g = 0.5mm$, and $\varepsilon_0 = 8.85 \times 10^{-12}$F/m, an inductance ($L_3$) value of 13.69 nH and capacitance (C_3) value of 255.08 pF were theoretically recorded. Hence, the f_{03} for the ground circular SRR structure is 2.69 GHz. The f_{03} with mutual coupling effect becomes 1.03GHz

III. DESIGN AND ANALYSIS OF SCM UNIT-CELL

In this section, the proposed SCM unit-cell is designed and experimentally analysed inside the waveguide structure. Further, the unit-cell is experimentally validated for DNG material behaviour.

TABLE 1. SCM design specifications.

Parameters	Dimension (mm)	Parameters	Dimension (mm)	Parameters	Dimension (mm)
a_1	23	b_3	0.5	c_5	111
a_2	22.5	b_4	1	c_6	9.75
a_3	0.5	b_5	0.5	c_7	7.75
a_4	1.5	b_6	46	c_8	0.5
a_5	0.5	b_7	23	c_9	0.5
a_6	8.5	b_8	0.5	d_1	130
a_7	9.0	b_9	46	d_2	111
a_8	0.5	c_1	46	d_3	13
a_9	0.5	c_2	0.5	d_4	15.25
b_1	5	c_3	0.5	d_5	13.5
b_2	4	c_4	130	d_6	13.5

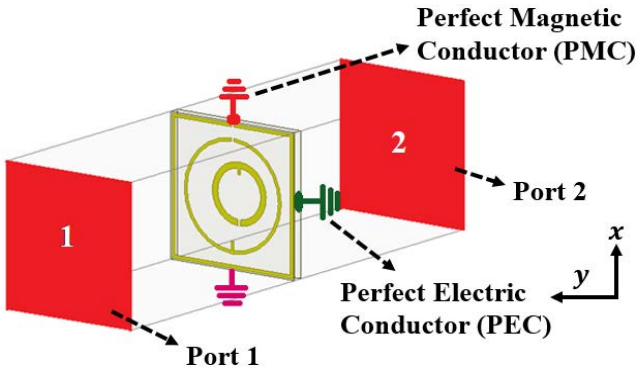

FIGURE 5. Simulation set up of the SCM unit cell.

A. DESIGN OF SCM UNIT-CELL

The proposed SCM unit-cell imported from HFSS software are depicted in Figure 4(a) and (b). The proposed SCM is designed on a 1.6mm thick FR-4 dielectric substrate with an overall dimension of 23 × 23mm^2. The substrate has a relative permittivity (ε_r) of 4.4 and a loss tangent ($\tan\delta$) of 0.02. The SCM unit-cell consists of one coupled square and circular SRR on the substrate, and a unit circular SRR on the ground plane of the substrate. The dimension of the outer square ring is 22.5 × 22.5mm^2 (0.0796λ × 0.0796λ) with a thickness of 1mm, and the gap between the square ring and the outer circle is around 5.6mm. The circular SRR which is placed on top of the substrate material has an outer radius of 9mm from the origin and a thickness of 0.5mm, whereas, the ground circular SRR has an outer radius of 5mm from the origin and a thickness of 1mm. The coupled square and circular rings produce the overall structure inductance, while the splits in the coupled SRR produce the total capacitance. An annealed copper having a conductivity (σ) of 5.8 × 10^7 S/m was used to construct the SCM structure.

TABLE 1 presents the complete parameter dimension of the proposed SCM structures in mm.

Figure 5 depicts the simulation/experiment setup of the SCM unit-cell. Here, the EM waves are distributed between waveguide ports 1 and 2, which are located at the positive and negative sides of the z-axis, respectively. To obtain the periodicity of the SCM unit-cell, the perfect electric conductor (PEC) boundary condition is applied to the sides of the unit-cell normal to E-field, and PMC (perfect magnetic conductor) to the sides normal to the H-field is applied. All SCM structures (unit-cell and array structures) presented in this paper will be confined by the same boundary conditions. For the simulation, a frequency range of 0.5 - 2 GHz was used. The radiation box is the simulation chamber, and its dimension is 23 × 23 × 70mm^3.

The proposed SCM unit-cell operates at TE$_{10}$ mode. The electric field distribution, and the propagation of EM wave inside the waveguide structure is illustrated in Figure 6.

The waveguide setup will provide the S-parameter data of the designed structure, and the same data will be utilized to retrieve the effective parameters such as 'ε', 'μ', and 'n'. The 'ε' and 'μ' are two important material qualities that determine how materials polarize in electric and magnetic fields.

To extract the properties of the MTM, several techniques, such as transmission-reflection (TR), Lossy-Drude, and Nicolson-Ross-Weir are used. In our study, the NRW technique was utilized to characterize the designed SCM structure. The values of effective permittivity (ε_{eff}), effective permeability (μ_{eff}), 'n', and wave impedance (z) are computed using the Eq (12) to Eq (15) (NRW simplified equations) [37]

$$\varepsilon_{eff} = \frac{n}{z} \tag{12}$$

$$\mu_{eff} = n.z \tag{13}$$

where,

$$n = \cos^{-1}\left(\frac{\left(1 - S_{11}^2 + S_{21}^2\right)}{2S_{21}}\right)/k\delta \tag{14}$$

and

$$z = \sqrt{\left[(1+S_{11})^2 - S_{21}^2\right]/\left[(1-S_{11})^2 - S_{21}^2\right]} \tag{15}$$

where k is the wavenumber, δ denotes slab thickness.

Figure 7 depicts a full five-step parametric simulation used to create the final unit-cell structure, with the last stage exhibiting significant transmission at 1.06 GHz. Figure 6(b) shows the simulated reflection coefficient (S_{11}) and transmission coefficient (S_{21}) of each stage in logarithmic and linear scales. As shown in steps 3 and 5, two open circuit stubs of

TABLE 2. The performance of the proposed unit-cell at various azimuthal angles.

Angle (φ)	Negative Permittivity (ε) range in GHz	Negative Permeability (μ) range in GHz	Negative Refractive Index (n) range in GHz	Amplitude at 1.06 GHz			BW of DNG (GHz)
				ε	μ	n	
$0^0 = 360^0$	0.68 TO 1.21	0.68 TO 1.22	0.68 TO 1.22	-4.96	-5.7	-5.3	0.53
60^0	0.575 TO 1.19	0.5 TO 1.19	0.5 TO 1.19	-6.8	-3.94	-5.2	0.615
120^0	0.598 TO 1.15	0.5 TO 0.175	0.54 TO 1.15	-2.3	-8.2	-5.0	0.65
180^0	0.5 TO 1.1	0.5 TO 1.1	0.5 TO 1.1	-1.2	-31.1	-5.7	0.61
240^0	0.5 TO 1.09	0.5 TO 1.14	0.5 TO 1.1	-10.5	-3.4	-7.5	0.61
300^0	0.5 TO 1.1	0.5 TO 1.1	0.5 TO 1.1	-1.8	-6.9	-6.1	0.6

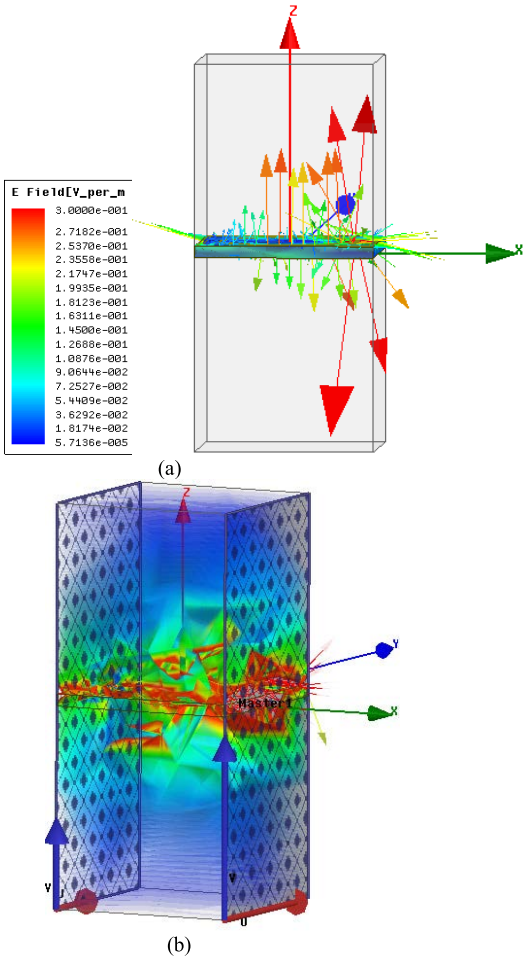

FIGURE 6. (a) Magnitude plot of SCM unit cell E-field distribution at Mode 1. (b) Magnitude plot of E-field distribution inside the waveguide at Mode 1.

2mm length are placed on the coupled SCSRR and the ground circular SRR.

In general, stubs are widely used in impedance matching circuits to correct for minor mismatches. An open-circuit stub of finite length 'l' will exhibit the capacitive behaviour if $\beta l < \frac{\pi}{2}$, and inductive behaviour if $\beta l > \frac{\pi}{2}$ (where β is the phase constant of transmission line). Both stubs have a βl value of 1.185, which is smaller than the $\frac{\pi}{2}$ (1.57), indicating that they are capacitive in nature. The addition of an open-circuit stub on the coupled SCSRR elevated the resonating frequency from 1.02GHz to 1.04GHz, as shown in the S_{11} and S_{21} plots of step 3, and another stub on the ground plane increased the resonating frequency from 0.99GHz to 1.06GHz, as shown in the S_{11} and S_{21} plots of step 5.

The proposed SCM unit-cell is rotated along the azimuthal plane from 0 to 360 degrees with a 60-degree interval, as shown in Figure 8, to further verify for DNG behavior. During these six stages, the values of effective characteristics such as 'ε', 'μ', and 'n' are recorded. From Figure 8(a) to (f), it is evident that in all six stages the proposed SCM exhibit negative characteristics throughout a frequency band of approximately 0.5 – 1.2 GHz and yield a DNG response at the designed frequency, that is at 1.06 GHz. As a result, the proposed SCM is considered as the double negative MTM, and it is very well suited for L-band applications. The performance of the SCM unit-cell is evaluated at various azimuthal angles, and the results are summarized in TABLE 2.

IV. RESULTS AND DISCUSSION

This section discusses the simulated and measured results of SCM unit-cells and the number of SCM array structures. Furthermore, the results of parametric analysis for various split widths, distance between rings, metal width of rings, and use of different substrate materials are thoroughly discussed.

A. FABRICATION SETUP

Figure 9 (a) to (e) depicts the fabricated SCM structures as well as the experimental setup for evaluating MTM characteristics. Both the SCM unit-cell and the 5 × 4 SCM array were measured using the same experimental setup. To determine the ω_m (magnetic resonance frequency) of the SCM structure, the EM wave transmission through the SCM unit-cell and the array structure must be measured. To measure the wave transmission through the unit-cell, it is placed between the two horn antennas, as shown in Figure 9(d).

The horn antenna and the unit-cell are separated by a distance of 10 cm. Initially, the transmission spectra are measured in free space and their values are recorded in the absence of SCM unit-cell. Next, the recorded data was

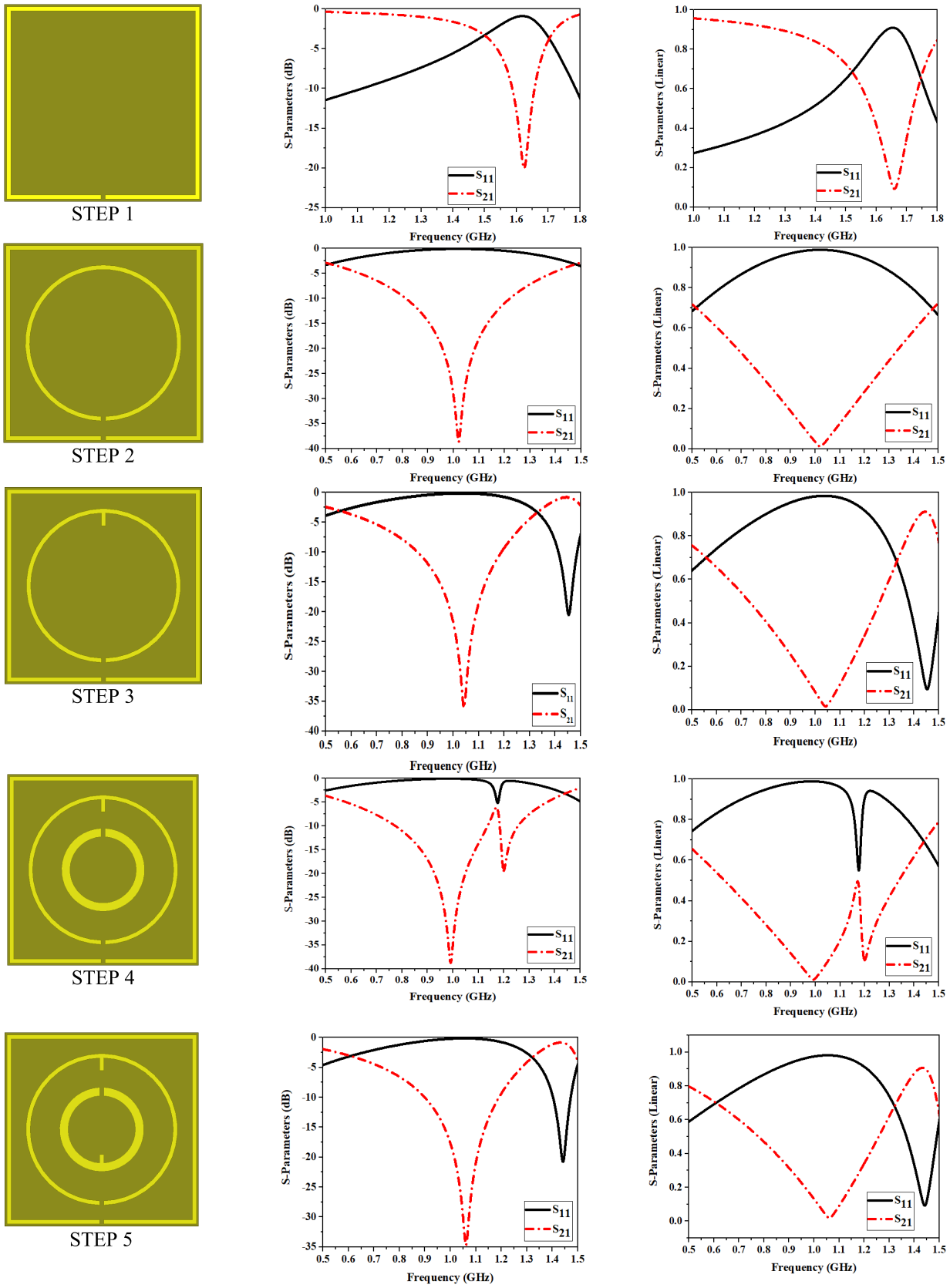

FIGURE 7. (a) Step-wise analysis of the SCM unit-cell structure. (b) S-Parameters in logarithmic scale (dB) and linear scale.

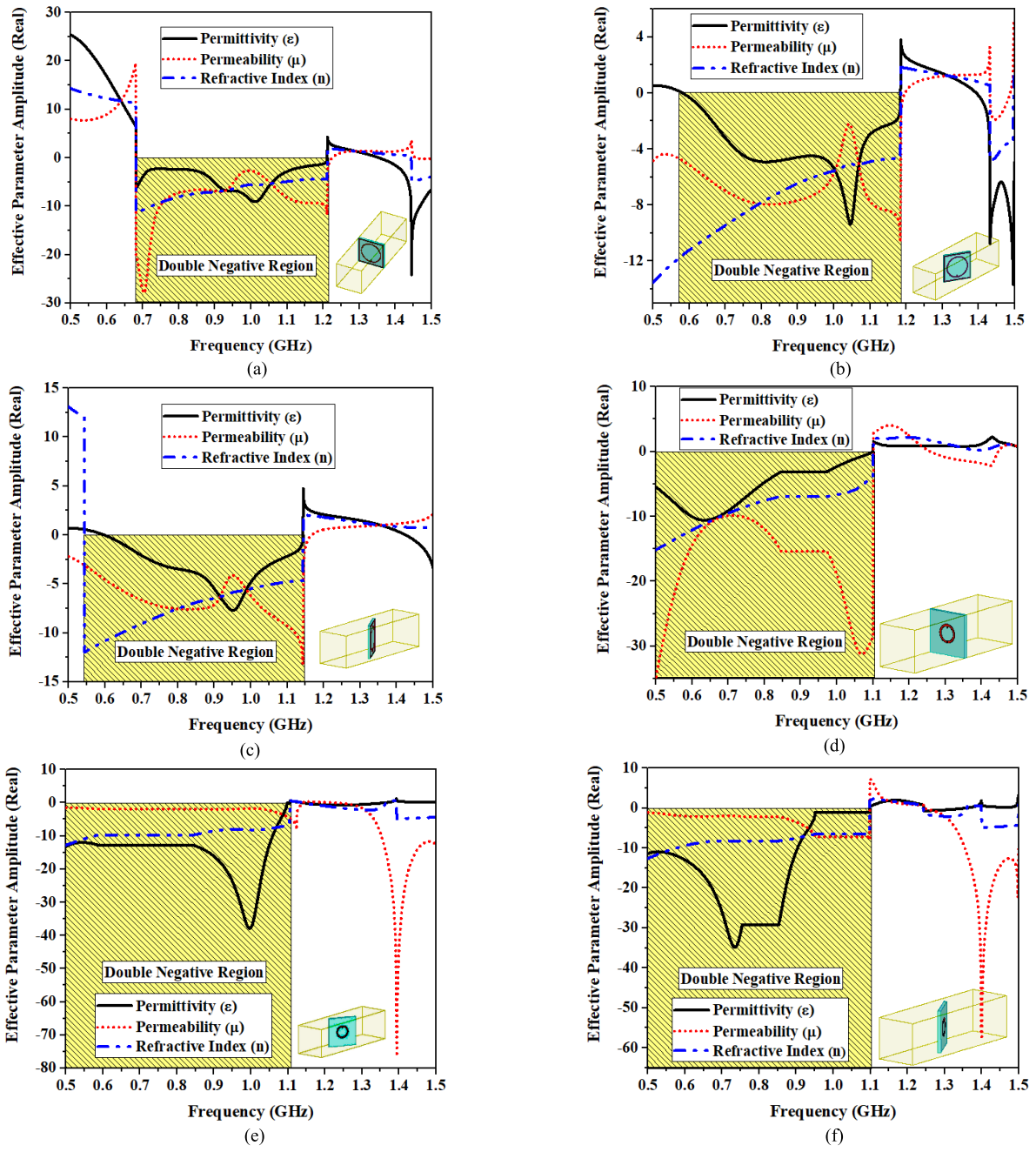

FIGURE 8. The amplitude values of the effective parameter (a) at 0° or 360° (b) at 60° (c) at 120° (d) at 180° (e) at 240° (f) at 300°.

utilized to regulate the Agilent N5247A vector network analyzer (VNA). After calibration, the proposed SCR unit-cell is placed between the horn antennas to measure EM wave transmission and reception. In this experiment, one horn antenna is used to transmit the EM wave, while the other is used to detect the MTM unit-cell response. The SCM array structure is also subjected to the same calibration and measurement procedures as depicted in Figure 9(e). In this case, the horn antenna and the array structure are separated by 15cm. In general, the antenna and the MTM structure are separated by a certain distance to ensure a minimum near-field effect on the transmission.

To reduce the sample edge effect, the distance between the horn antenna and the sample (SCM unit-cell or Complete slab) must be carefully calibrated to project the majority of the incident wave within the region covered by the sample. Furthermore, a precise separation distance is essential for measuring parameters such as transmission and reflection coefficients with a high SNR (Signal to noise ratio).

B. SCM UNIT-CELL ANALYSIS

Figure 10 (a) to (d) illustrates the scattering parameter results such as S_{11}, S_{21}, and the effective medium results including 'ε', 'μ', and 'n' for SCM unit-cell. As depicted

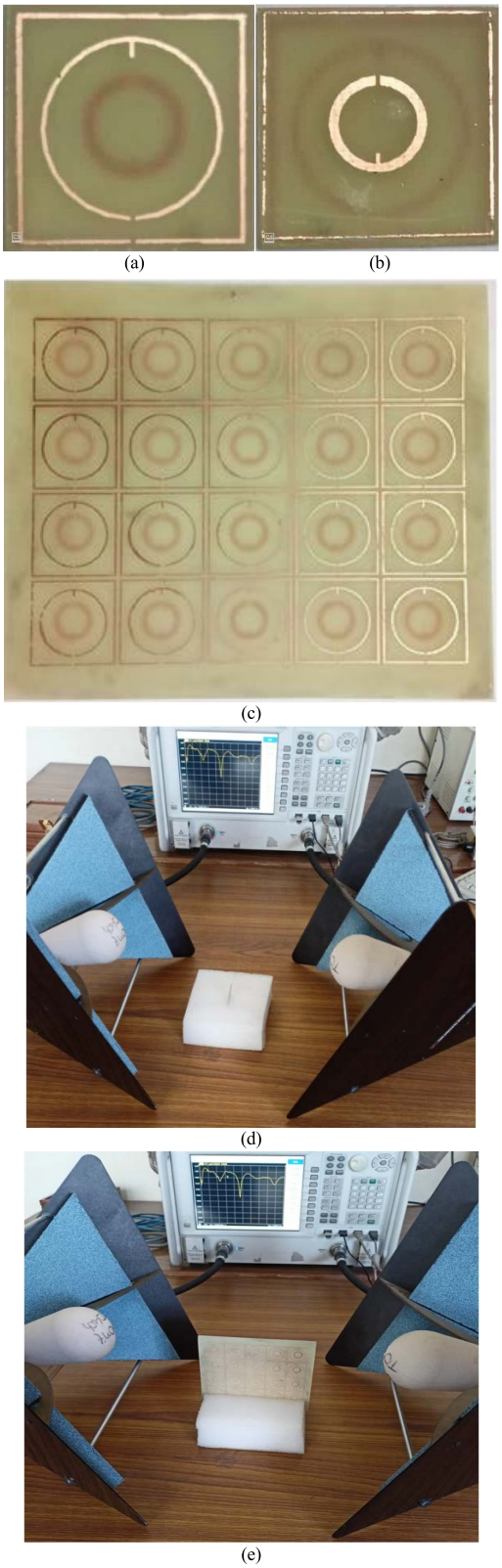

FIGURE 9. Fabricated SCM structures (a) top-view of the SCM unit-cell, (b) bottom-view of the SCM unit-cell, (c) 5 × 4 SCM array, and (d) experimental setup for unit-cell and 5 × 4 array.

in Figure 10(a), the simulated SCM unit-cell resonates at 1.06 GHz with a magnitude of −35.02 dB, whereas the measured SCM resonates at 1.06 GHz with a magnitude of −32.38 dB. This implies that the experimental and simulated results agree well.

A small discrepancy in magnitude and the frequency of the measured and simulated results is observed in the Figure 10(a). The resonances around 0.6 to 0.7GHz and 1.4 to 1.5GHz exhibit a frequency discrepancy between the simulated and measured results, which may be due to the addition of manufacturing and calibration errors with the mutual coupling effect between two waveguide ports. Despite these discrepancies, the fabricated result closely resembles the simulated outcome. The difference between simulated and measured results is also affected by the type of substrate material, with approximately 5% experimental error being acceptable for lossy substrate materials [38], [39].

In general, the difference between simulated and measured data could be caused by one of the following factors:

i. Calibration error of the Agilent N5247A vector network analyzer (VNA)

ii. Minor flaws in the fabrication process

iii. Effect of the mutual resonance across the transmitting and receiving waveguide ports will always modify the interpretations and cause minor variation in both data.

iv. The dielectric constant of the substrate material has a considerable impact on the measurement data. In general, the substrate permittivity will always influence the resonating frequency. In general, the permittivity of the substrate will always have an effect on the resonating frequency. The increase in permittivity will slightly drag the peak resonance points towards the lower frequencies. Furthermore, the permittivity variation will also affect the capacitance values between the ground plane and the radiating patch.

v. The difference between the transmission and the reflection coefficient, along with frequency shift and the break in resonating frequency, is primarily caused by the fact that not all of the incoming power will be reflected or transmitted.

The real permittivity value reaches negative at 0.68 GHz as illustrated in Figure 10 (b), and the negative region has been extended up to 1.21 GHz. The permittivity value of −4.96 dB is recorded at the resonating frequency. The real permeability value falls below zero at 0.67 GHz with a −21.9 dB amplitude, as shown in Figure 10 (c), and the negative zone has been extended up to 1.25 GHz. The peak permeability value of −28.9 dB is recorded at 0.71 GHz, whereas at the resonating frequency, the permeability value is −5.7 dB. Furthermore, the proposed SCM unit-cell exhibits LHM characteristics in the frequency range of 0.67 GHz to 1.21 GHz, as shown in Figure 10 (d). Hence, the proposed SCM structure is well suited for aircraft surveillance applications.

The effective medium ratio (EMR) defines the compactness of any MTM structure [40]. The EMR is defined as the ratio of the wavelength to the length of the MTM unit-cell, as given in Eq (16). To accomplish the double negative

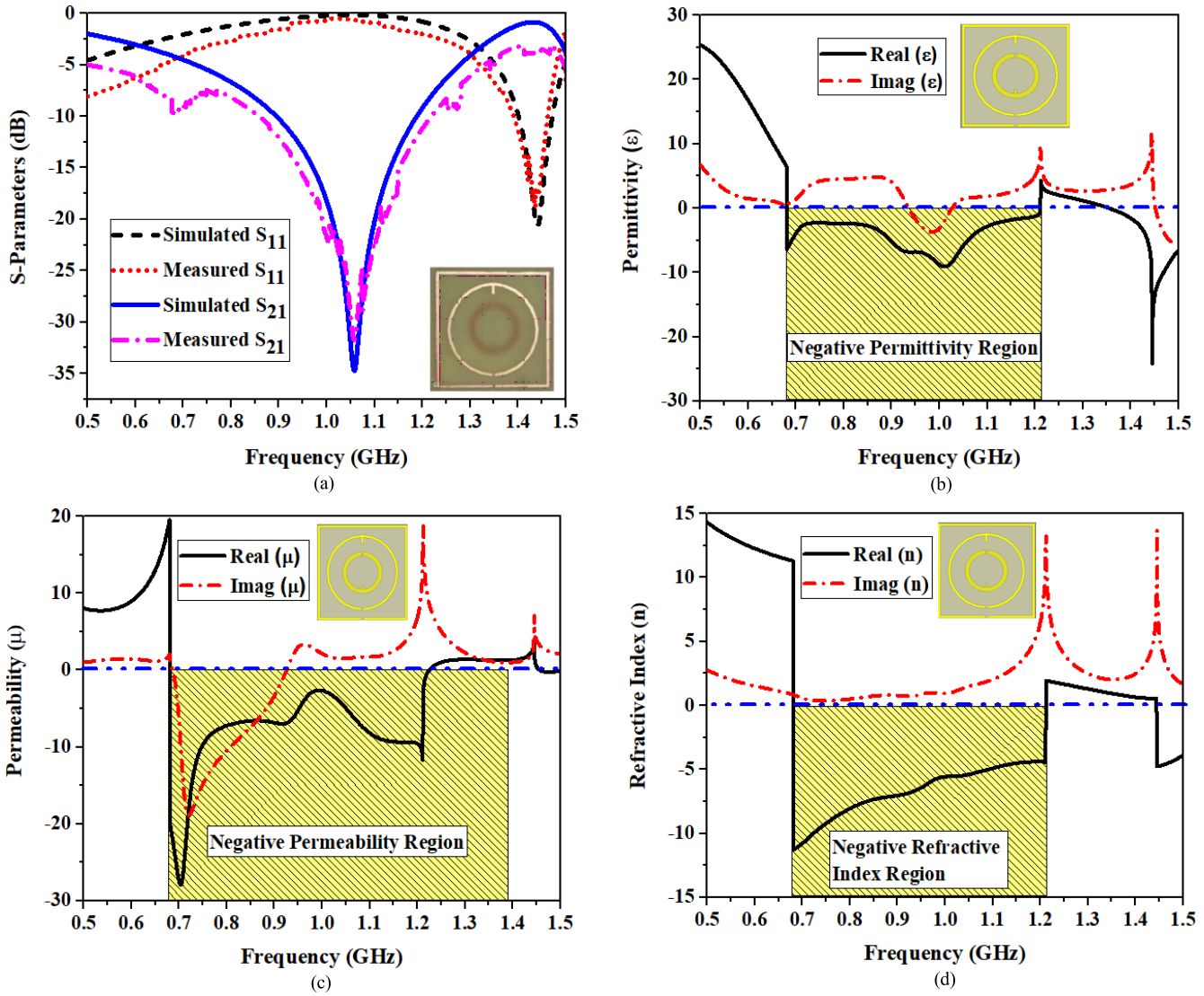

FIGURE 10. Quantitative findings of (a) simulated and measured S-parameters, (b) permittivity (ε), (c) permeability (μ), and (d) refractive index (n).

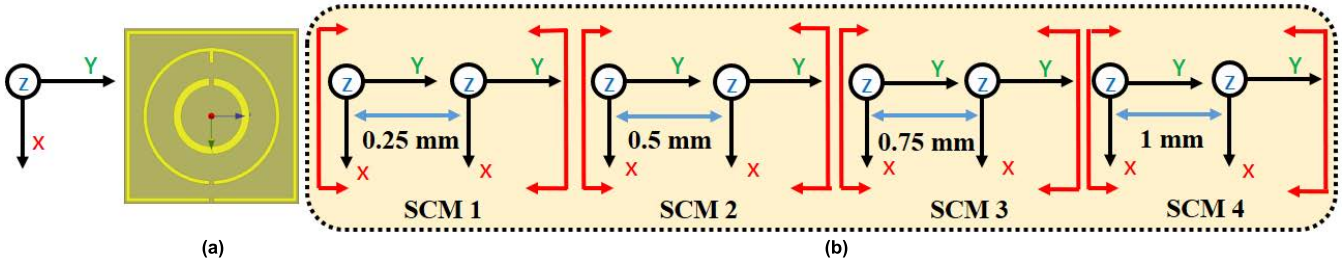

FIGURE 11. (a) Axial structure. (b) Coupling distance analysis for 1 × 2 SCM array structure.

characteristics in the designed MTM unit-cell, the EMR value should always be greater than 4. For the proposed SCR unit cell, the EMR value is 12.57.

$$EMR = \frac{Wavelength\ (\lambda)}{Length\ of\ unit\ cell\ (L)} \tag{16}$$

C. MUTUAL COUPLING ANALYSIS

This section discusses the various inter-unit cell coupling effects for 1 × 2 and 2 × 2 SCM array structures. Figure 11 depicts four identical 1 × 2 SCM array structures with varying mutual coupling distances. The coupling distance between SCM unit-cell is varied from 0.25mm to 1mm,

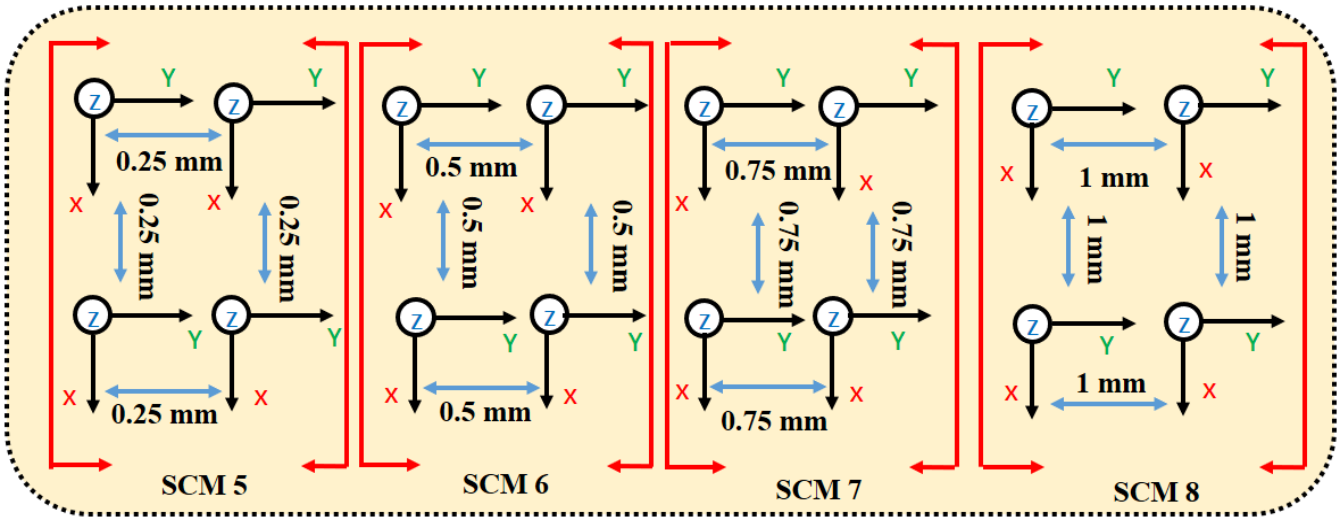

FIGURE 12. Coupling distance analysis for 2 × 2 SCM array structure.

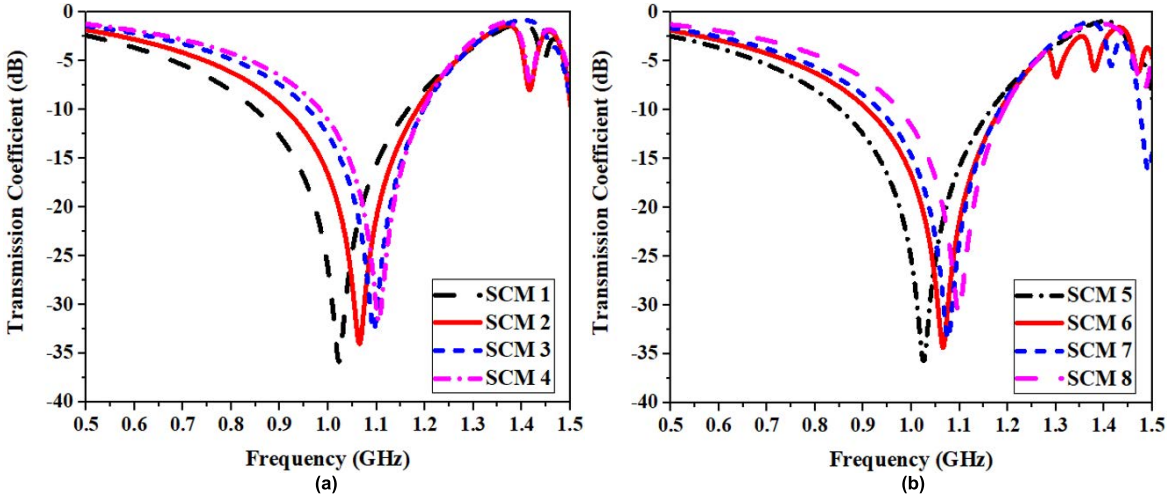

FIGURE 13. Transmission coefficient plot for (a) 1 × 2 SCM array structure and (b) 2 × 2 SCM array structure.

and as the separation distance increases from 0.25mm to 1mm with an interval of 0.25mm, there is a significant increase in the resonating frequency as illustrated in Figure 13(a). The 1 × 2 SCM array structure resonates at 1.06GHz with a reflection coefficient of −34.10 dB when the unit-cells are separated horizontally by 0.5mm coupling distance. In meta-material, short range coupling between unit-cell occurs because of the nearest resonator. In the case of a 2 × 2 SCM array, the four structures (SCM 5 to SCM 8) are identical in shape but separated by different horizontal and vertical coupling distances as depicted in Figure 12. As shown in Figure 13(b), the horizontal and vertical distances are varied from 0.25mm to 1mm with 0.25mm intervals to determine the effect of mutual coupling on the resonating frequency. Several combinations of horizontal and vertical coupling distances are examined to establish the best mutual coupling, and when the unit-cells are separated by 0.5mm coupling distance (horizontally and vertically), the 2 × 2 SCM array resonates at 1.06GHz with a reflection coefficient of −34.30 dB. As a result, the same coupling distance is maintained even for the 5 × 4 SCM array structure.

D. SCM ARRAY ANALYSIS

In this section, various array configurations of the proposed SCM structure are discussed. Since a single MTM unit-cell cannot manifest the rational exotic electromagnetic behavior, several sets of SCM array structures, such as 2 × 1, 2 × 2, and 5 × 4, are designed and analyzed for both S-parameters and effective parameters. The same simulation and analysis approach that was utilized for the SCM unit-cell was adopted for all of the proposed SCM array structures.

1) SCM ARRAY (2 × 1)

Figure 14 (a) depicts the simulated structure of a 2 × 1 SCM array. The overall dimension of the structure is 46 × 23 mm^2 (0.165λ × 0.0815λ). The two unit-cells

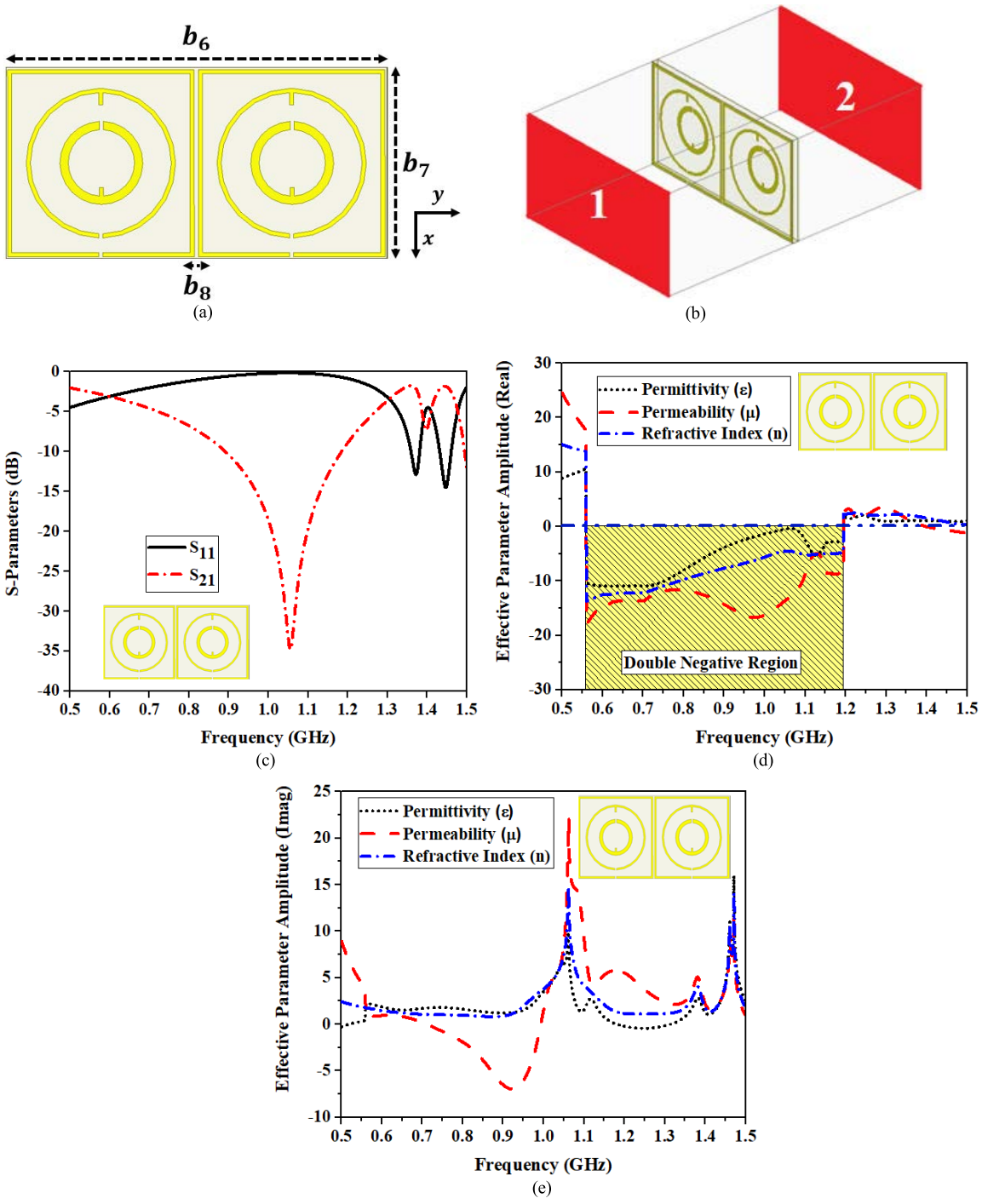

FIGURE 14. SCM array design: (a) 2 × 1 SCM structure, (b) simulation setup, (c) simulated S-parameter plot, (d) real effective parameter plot, and (e) imaginary effective parameter plot.

are separated by a distance of 1mm. Figure 14(b) shows the simulation setup for retrieving the S-parameters. Figure 14(c) depicts the recorded S-parameter values of a 2 × 1 SCM array, demonstrating that the array structure resonates at 1.06 GHz with a magnitude of −34.8 dB. The simulated data is then utilized to extract the effective parameters of the SCM array structure.

As illustrated in Figure 14 (d), the real 'ε', 'μ', and 'n' values for a 2 × 1 SCM array becomes negative at 0.56 GHz, with amplitudes of −11.04 dB, −18.01 dB, and −14.98 dB, respectively. The amplitude values of 'ε', 'μ', and 'n' for the designed frequency are −0.91 dB, −14.80 dB, and −5.08 dB, respectively, at the resonating frequency. Figure 14(e) depicts the imaginary plot of the effective parameters.

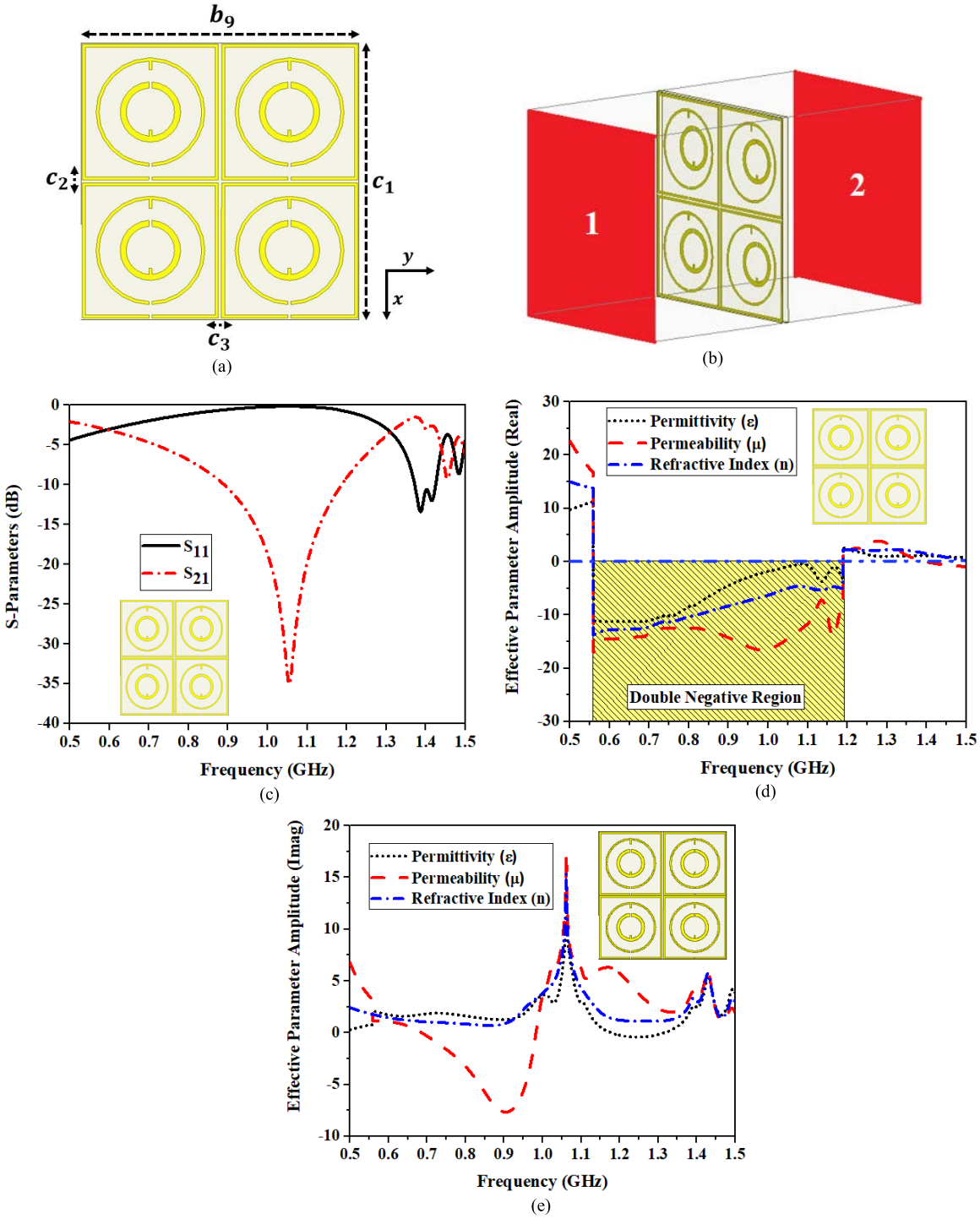

FIGURE 15. SCM array design: (a) 2 × 2 SCM structure, (b) simulation setup, (c) simulated S-parameter plot, (d) real effective parameter plot, and (e) imaginary effective parameter plot.

The array has a double negative region for the frequency band of 0.55 - 1.19 GHz.

2) SCM ARRAY (2 × 2)

Figure 15 (a) depicts the simulated structure of a 2 × 2 SCM array. The overall dimension of the structure is 46 × 46 mm^2 (0.165λ × 0.165λ). The unit-cells are separated by 1mm on both the horizontal and vertical axes. Figure 15 (b) shows the simulation setup for retrieving the S-parameters. A frequency spectrum of 0.5 - 2 GHz was used for the simulation.

Figure 15 (c) depicts the recorded S-parameter values of a 2 × 2 SCM array, demonstrating that the array structure resonates at 1.06 GHz with a magnitude of −35.2 dB. The simulated data is then utilized to attain the effective parameters of

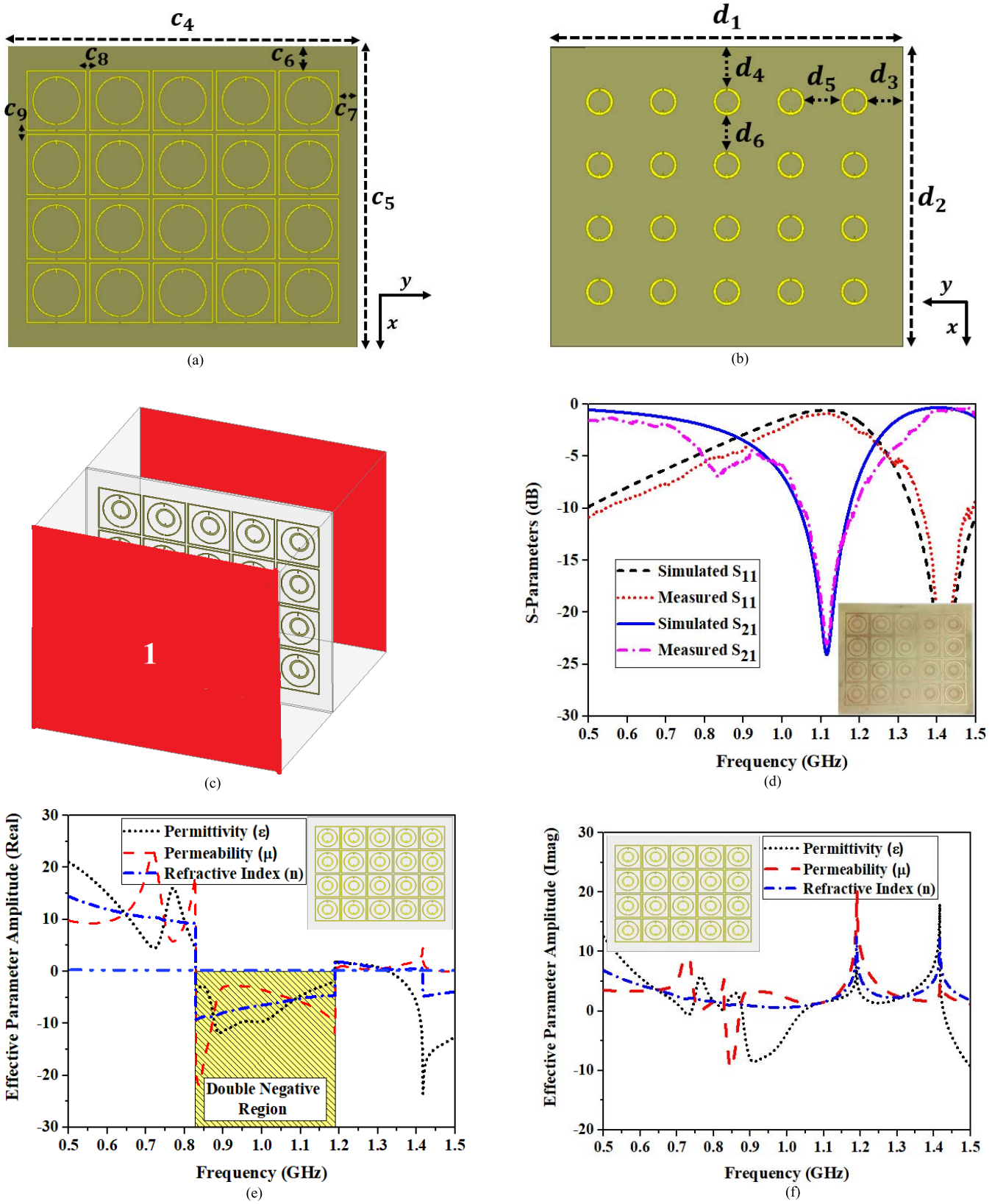

FIGURE 16. SCM array design: (a) top and (b) bottom view of 5 × 4 SCM structure, (c) simulation setup, (d) simulated and measured S-parameters, (e) real effective parameter plot, and (f) imaginary effective parameter plot.

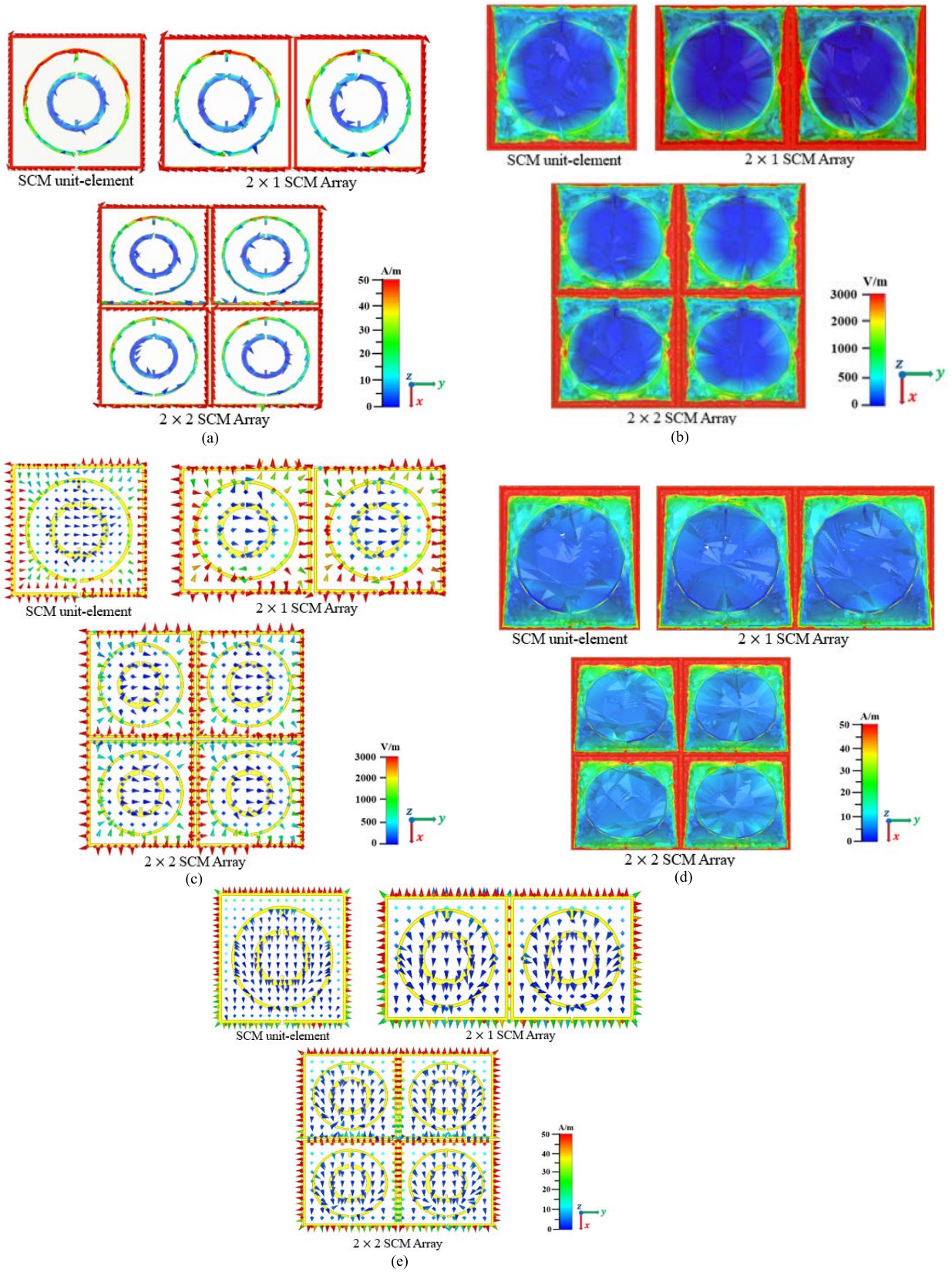

FIGURE 17. (a) Surface current distribution. (b) E-field distribution. (c) Vector representation of E-field distribution. (d) H-field distribution. (e) Vector representation of H-field distribution for SCM unit-element, 2 × 1 and 2 × 2 SCM array.

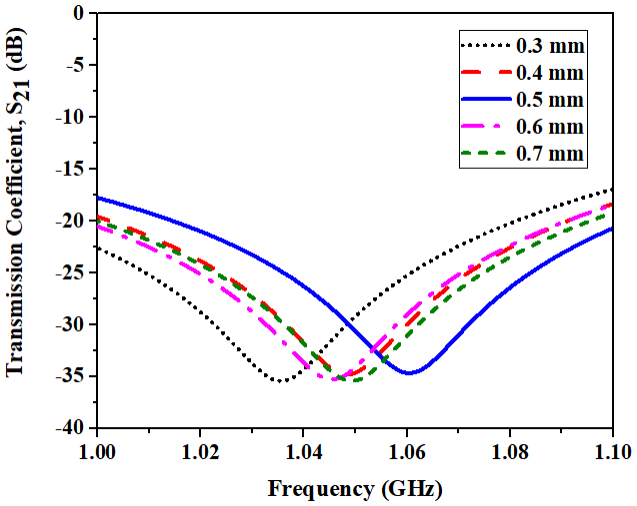

FIGURE 18. The S_{21} plot for different split width.

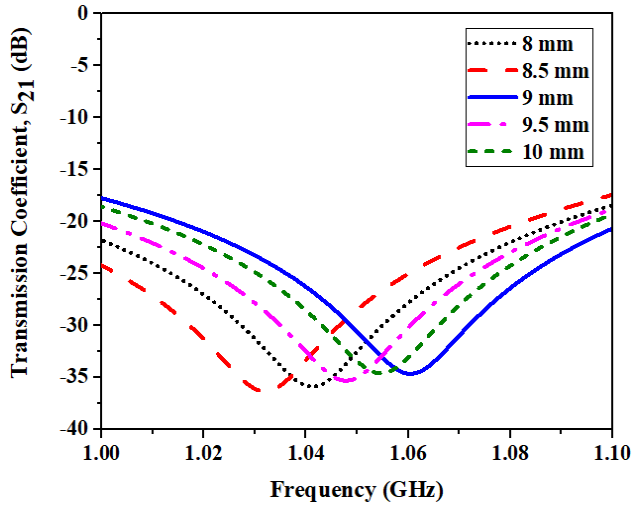

FIGURE 19. The S_{21} plot for gap between coupled square and circular ring.

the SCM array structure. As depicted in Figure 15(d), the real 'ε', 'μ', and 'n' values for a 2 × 2 SCM array become negative at 0.56 GHz, with amplitudes of −12.21 dB, −18.08 dB, and −14.62 dB, respectively. The amplitude values of 'ε', 'μ', and 'n' for the designed frequency are −1.04 dB, −15.18 dB, and −6.09 dB, respectively. Figure 15(e) depicts the imaginary plot of the effective parameters. The array has a double negative region for the frequency band of 0.55 - 1.19 GHz.

3) SCM ARRAY (5 × 4)

The top and bottom-view of the proposed 5 × 4 SCM array structure imported from HFSS software are depicted in Figure 16(a) and (b). The overall dimension of the structure is 130 × 111 mm^2.

All the unit-cells are separated by 1mm on both the horizontal and vertical axes. Figure 16 (c) shows the simulation

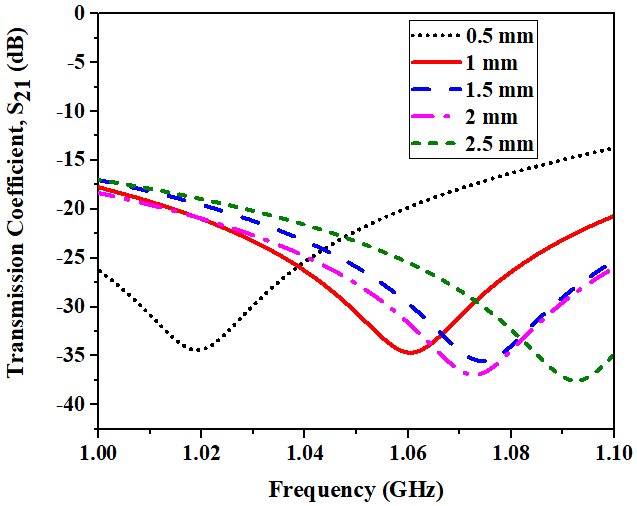

FIGURE 20. The S_{21} plot for different square and circular ring width.

setup for retrieving the S-parameters. A frequency spectrum of 0.5 - 2 GHz was used for the simulation. As depicted in Figure 16 (d), the simulated 5 × 4 SCM array resonates at 1.06 GHz with a magnitude of −24.2 dB, whereas the measured SCM resonates at 1.06 GHz with a magnitude of −22.8 dB. The simulated data is then utilized to find the effective parameters of the SCM array structure. As shown in Figure 16 (e), the real 'ε', 'μ', and 'n' values for a 5 × 4 SCM array become negative at 0.83 GHz, with amplitudes of −4.98 dB, −21.83 dB, and −9.81 dB, respectively. The amplitude values of 'ε', 'μ', and 'n' for the designed frequency are −7.12 dB, −4.99 dB, and −5.90 dB, respectively. The imaginary plot of the effective parameters is illustrated in Figure 16 (f). This structure has a double negative region for the frequency band of 0.83 - 1.19 GHz.

Figure 17 depicts the surface current, electric (E) and magnetic (H) field distributions, and vector representations of the E and H field distributions of the proposed NRI-MTM at 1.06GHz. The surface current distribution depicts the scattering of electrical current caused by the applied electromagnetic (EM) fields. The density of the surface current is maximum at the outer SRR and the upper surface of the subsequent circular SRRs, as shown in Figure 17(a). Since the two ring (Outer SRR and Inner SRR) currents are parallel, it tries to strengthen the H-field formed by them, resulting in a strong coupled H-field encircling these two rings, as seen in Figure 17(d). In addition to H-field, the density of E-field is particularly high in the region of the two outer SRR. The strong E and H-field around the outer SRR causes E and H resonance, which leads to resonances in scattering variables at the operating frequency.

The dependence of the H-field on the current density may be evaluated by comparing the distribution of the H-field along with the current density. By carefully inspecting the E-field distribution as illustrated in Figure 17(b), it is clear that the E-field distribution is strongly connected to the rate of change of the H-field, implying that a high E-field

distribution is observed wherever the rate of change of the H-field is high. As a result, it satisfies the E and H-field relation stated by Maxwell's equation [41]. Hence, the contribution of various parts of the resonator to the EM properties allows S_{21} to resonate at the desired frequency. The moderate current distribution is observed at the split of the circular SRR placed on the ground plane. The E-field distribution and its vector representation for SCM unit-cell, 2 × 1 SCM array, and 2 × 2 SCM array at the resonant frequency are shown in Figure 17(b). The E-field distribution is particularly dense on both sides, the bottom surface of the square SRR, and around the split of the circular SRR. The field distribution is moderate on all sides and the bottom surface of the circular SRR.

The vector plot represents the direction of field dispersion. As depicted in Figure 17(c), the field movement of the proposed SCM unit-cell is clockwise on the top side and anticlockwise on the bottom side, and a similar field distribution has been observed for the array structures as well. The H-field distribution on the proposed structures is depicted in Figure 17(d), and the H-field distribution is very dense on both sides, as well as on the top surface of the square SRR and the upper half of the circular SRR. The field distribution is moderate on either sides of the circular SRR. As seen in Figure 17(e), the scattered H-field begins to flow in the same direction and accumulates at the split or gap between the circular and square SRRs. As shown in Figure 17(b) & (d), the E and H-fields display opposite excitation at the resonant frequency, hence the proposed NRI-MTM (unit-cell, 1 × 2 SCM array, and 2 × 2 SCM array) fulfils the Maxwell equation [39], [42], [43].

The performance of the proposed SCM structures is summarized in TABLE 3.

E. PARAMETRIC STUDY

The proposed SCM unit-cell has been simulated multiple times to ensure the optimum MTM performance. Initially, the square ring was chosen as the outermost ring, and then the proposed SCR structure was developed using the trial and error approach. Four parametric analyses were conducted in order to understand the design constraints and to determine the best structure for the MTM.

1) PARAMETRIC ANALYSIS OF SPLIT WIDTH

The proposed SCR unit-cell design includes three splits of the same width. Two splits are etched on the coupled square and circular ring that is placed on the substrate, and one split is etched on the circular ring which is placed on the ground plane. As depicted in Figure 18, the split gap was varied from 0.3 mm to 0.7 mm, and the corresponding transmission coefficient (S_{21}) and the resonating frequency for each width are recorded. In theory, increasing the split gap reduces the overall capacitance, resulting in a higher resonating frequency. From the simulated results, it is clear that the split width had an effect on the (S_{21}) as well as the resonating frequency. For the proposed structure, the split width of 0.5 mm is chosen, and an S_{21} of −34.8 dB at 1.06 GHz has been recorded for this width. TABLE 3 shows the simulated values of S_{21} and their corresponding frequencies for various split widths.

TABLE 3. Recorded values of S_{21} and resonating frequency for different split widths.

Split Width (mm)	S_{21} (dB)	Frequency (GHz)
0.3	-35.9	1.036
0.4	-34.8	1.049
0.5	**-34.8**	**1.06**
0.6	-35.9	1.046
0.7	-35.9	1.05

TABLE 4. Recorded values of S_{21} and resonating frequency for different square and circular ring gap.

Ring gap (mm)	S_{21} (dB)	Frequency (GHz)
8	-36.1	1.042
8.5	-36.9	1.032
9	**-35**	**1.06**
9.5	-35.3	1.048
10	-35	1.053

2) PARAMETRIC ANALYSIS OF THE GAP BETWEEN THE SQUARE AND CIRCULAR RINGS

As shown in Figure 19, the spacing between the square and circular rings was varied from 8 mm to 10 mm, and the corresponding simulated values of S_{21} and resonating frequency for each gap variation were recorded. Increased distance between consecutive rings reduces overall capacitance and inductance, resulting in a rise in resonating frequency. From the simulated results, it is clear that the gap between the consecutive rings has a major influence on the resonating frequency but a negligible effect on the S_{21}. For the proposed structure, the consecutive rings are separated by a distance of 9 mm, and an S_{21} of −35.01 dB at 1.06 GHz has been recorded for this width. TABLE 4 shows the simulated values of S_{21} and their corresponding frequencies for various ring gaps.

3) PARAMETRIC ANALYSIS OF THE WIDTH OF THE SQUARE AND CIRCULAR RINGS

In theory, increasing the split ring widths reduces the overall mutual capacitance and inductance, resulting in a higher resonating frequency. As illustrated in Figure 20, the ring width was varied from 0.5 mm to 2.5 mm, and the corresponding simulated values of S_{21} and resonating frequency for each ring width variation were recorded. From the simulated results, it is clear that the ring width has a significant effect on both resonating frequency and S_{21}. For the proposed structure, the ring width of 1 mm was chosen, and an S_{21} of −34.98 dB at 1.06 GHz has been recorded for this width.

TABLE 5. Recorded values of S_{21} and resonating frequency for different square and circular ring width.

Ring Thickness (mm)	S_{21} (dB)	Frequency (GHz)
0.5	-34.98	1.019
1	**-34.98**	**1.06**
1.5	-35.92	1.074
2	-37.42	1.067
2.5	-37.55	1.092

TABLE 5 shows the simulated values of S_{21} and their corresponding frequencies for various ring widths.

4) PARAMETRIC ANALYSIS OF DIFFERENT SUBSTRATE MATERIALS

The proposed SCM unit-cell has been designed on two different dielectric substrate materials: FR-4 and Rogers RT5880 lossy material. The FR-4 has a loss tangent (LT) of 0.02 and a relative permittivity (RP) of 4.4, whereas the Rogers RT5880 has an LT of 0.0009 and an RP of 2.2. For the parametric analysis, the SCM structure and substrate material dimensions remained unchanged.

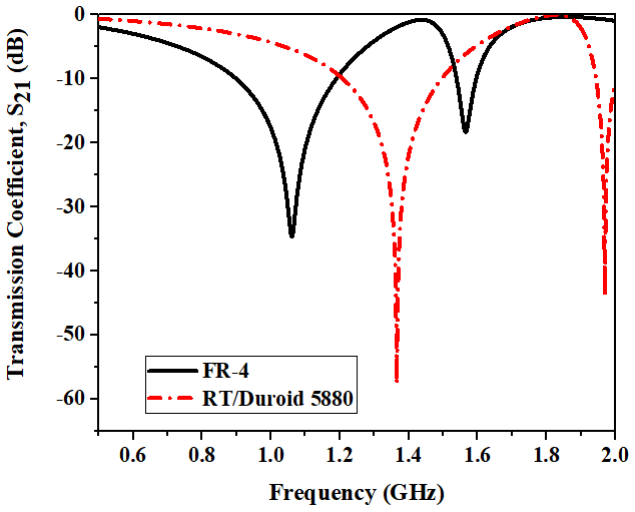

FIGURE 21. The S_{21} plot for different substrate material.

The simulated results, as shown in Figure 21, demonstrate that changing the substrate material has a substantial impact on both the resonating frequency and the S_{21} value. The SCM structure on FR-4 substrate material resonates at 1.06 GHz with an S_{21} value of -34.65 dB, whereas the design on RT/Duroid 5880 resonates at 1.367 GHz with an S_{21} value of -48.56 dB. TABLE 6 shows the simulated values of S_{21} and their corresponding frequencies for different substrate materials.

Finally, considering the cost and availability of the material, FR-4 was chosen as the substrate material in our research rather than RT/Duroid 5880.

TABLE 6. Recorded values of S_{21} for different substrate material.

Substrate Material	S_{21} (dB)	Frequency (GHz)
FR-4	**-34.65**	**1.06**
RT/Duroid 5880	-48.56	1.367

TABLE 7. Optimal dimensions of the proposed RMPA.

Parameter	Dimension(mm)	Parameter	Dimension(mm)
e_1	130	e_5	1
e_2	111	e_6	33
e_3	114	e_7	43
e_4	91	e_8	9

F. ANALYSIS OF THE PROPOSED NRI-MTM FOR PERFORMANCE IMPROVEMENT OF TCAS ANTENNA

In this section, a rectangular microstrip patch antenna (RMPA) for 1.06 GHz is designed to study the effect of the proposed NRI-MTM on antenna performance especially gain and bandwidth.

1) ANTENNA DESIGN

As discussed in Section III, the proposed SCM exhibits negative 'ε', 'μ', and 'n'. The properties of DNG have vast applications in the antenna field for enhancing the performance, and in many research works, the DNG material is utilized as a superstrate to enhance the antenna gain and bandwidth. Hence, in order to assess the proposed NRI-MTM, an RMPA resonating at 1.06GHz is designed using HFSS software as illustrated in Figure 22.

TCAS is a surveillance system mandated in all aircrafts to prevent air accidents. It utilizes a directional antenna to monitor any nearby aircrafts. The frequency band of 960-1215MHz is allotted for the TCAS/aircraft surveillance applications. TCAS employs 1.03GHz radio frequency to send the inquiry signal for examining the range and location of all neighboring aircraft, and 1.09GHz radio frequency to receive the response of nearby aircraft. Hence, the RMPA is designed for 1.06GHz, which is the central frequency of the TCAS antenna.

As shown in Figure 22 (a), the microstrip feedline with inset-cut feeding method is utilized to feed the antenna, and the ground plane is a complete copper as shown in Figure 22(b). The RT/Duroid 5880 substrate material with a loss tangent ($\tan\delta$) $= 0.0009$, relative permittivity (ε_r) $= 2.2$ is used to simulate the RMPA. The overall dimension of the RMPA is $114 \times 91 \times 3\text{mm}^3$. The optimized antenna dimension is given in TABLE 7. The RMPA resonates at 1.06 GHz with -19.52 dB reflection coefficient, and 13.10MHz (1.0609-1.074GHz) bandwidth, which is depicted in Figure 23. The antenna gain plot is depicted in Figure 24, and the proposed RMPA has a maximum gain of 4.60 dB.

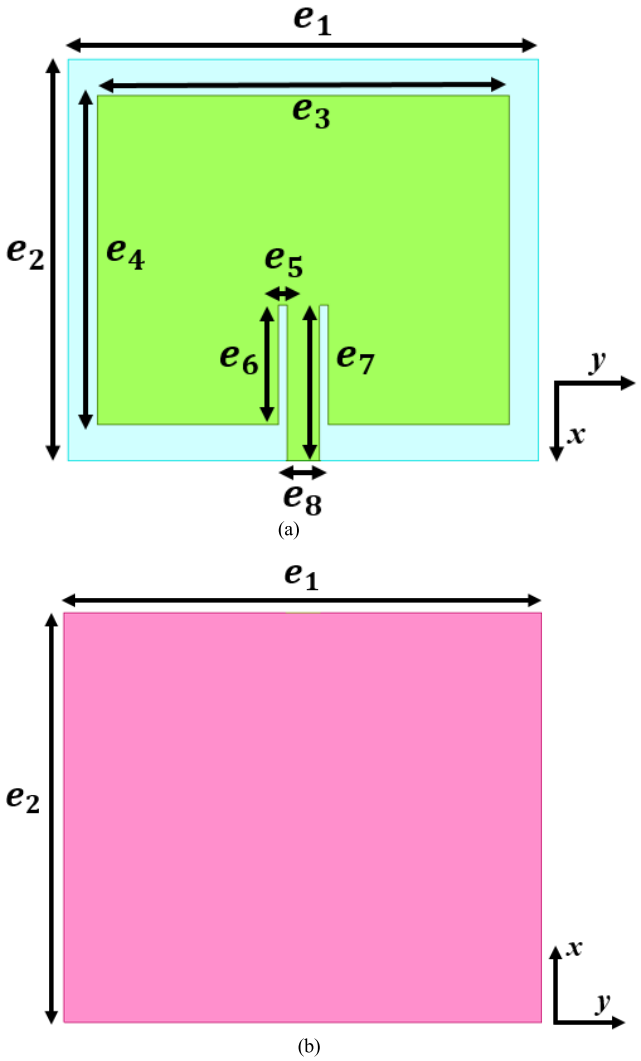

FIGURE 22. The proposed RMPA (a) top-view (b) ground plane (bottom-view).

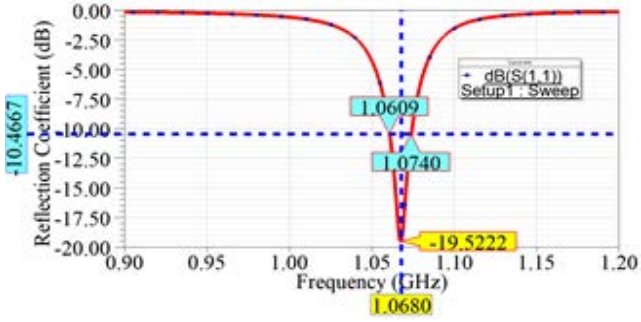

FIGURE 23. Reflection coefficient graph of proposed RMPA.

2) NRI-MTM LOADED ANTENNA

The NRI-MTM slab is placed on the proposed RMPA to analyze its effect on the antenna gain as illustrated in Figure 25. Since the dimension of the metamaterial slab is same as RMPA, it completely covers the antenna. After placing the 5×4 SCM array on the RMPA, the design has been simulated

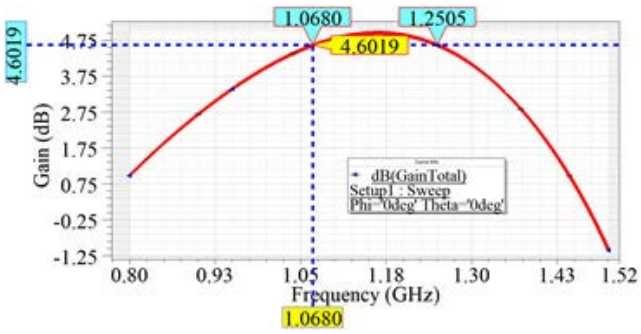

FIGURE 24. Gain plot of proposed RMPA.

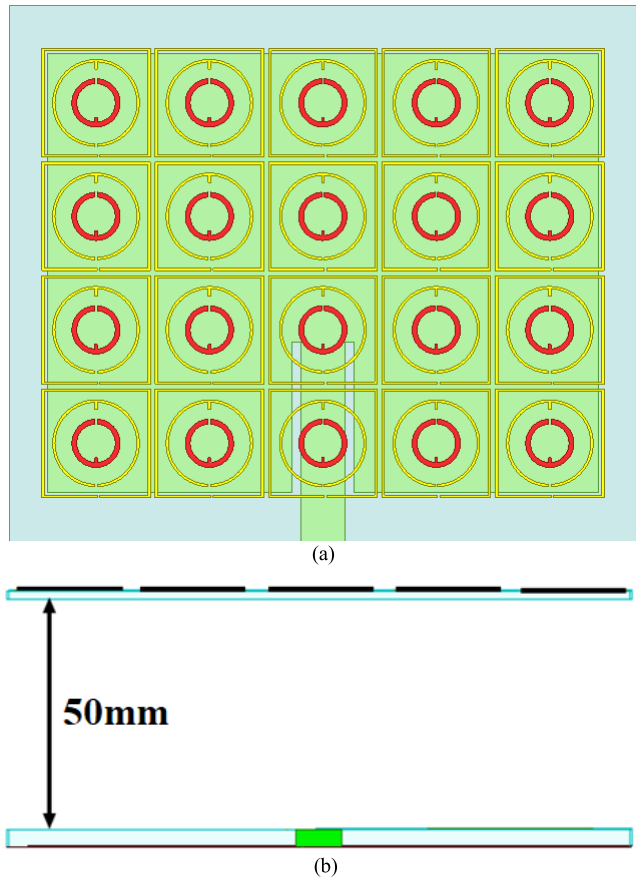

FIGURE 25. Proposed RMPA loaded with NRI MTM cover (a) top-view and (b) side-view.

multiple times to find the optimum distance between the RMPA and the MTM slab. The better result has been noticed when the NRI-MTM slab is kept at 50mm distance from the RMPA. The effect of distance between the RMPA and the NRI-MTM slab on the reflection coefficient and antenna gain is depicted in Figure 26 and 27, respectively.

The distance between the radiating patch and the metamaterial superstrate is generally called as resonant distance (h), and it is given by [44], [45]

$$h = \frac{\varphi_1 + \varphi_2}{\pi}\frac{\lambda}{4} + N\frac{\lambda}{2}, \quad N = 0, 1, 2 \ldots \tag{17}$$

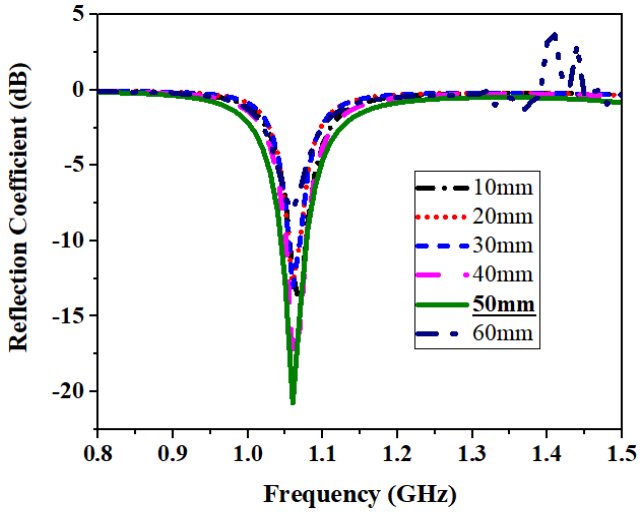

FIGURE 26. The effect of distance between RMPA and NRI-MTM cover on reflection coefficient.

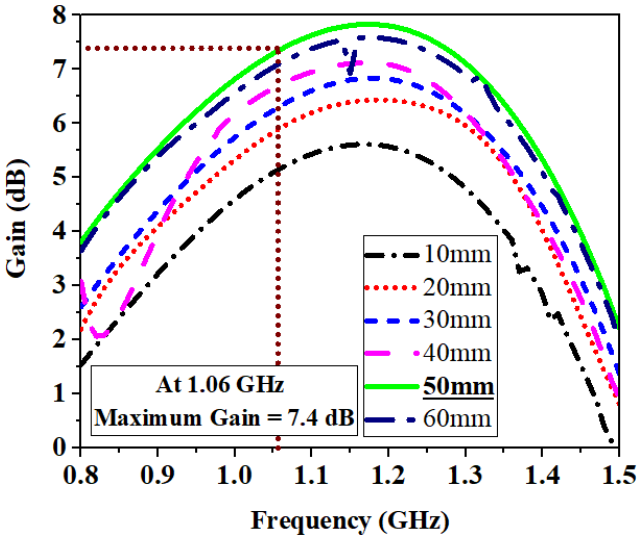

FIGURE 27. The effect of distance between RMPA and NRI-MTM cover on gain.

where φ_1 is reflection phase of the ground plane, φ_2 is reflection phase of the metamaterial, and λ is operating wavelength.

Since the ground plane of the radiating patch is a metallic conductor, its reflection phase is close to $\pi(\varphi_1 = \pi)$, hence the Eq. can be reduced to

$$h = \left(1 + \frac{\varphi_2}{\pi}\right)\frac{\lambda}{4} \tag{18}$$

For 1.06GHz resonating frequency, the operating wavelength becomes 283mm, and the reflection phase of the radiating patch can be varied from 0 to π. Hence, the maximum distance between radiator and the superstrate layer is $\lambda/2$. In our work, the maximum gain of 7.4 dB is obtained when the distance between radiating patch and the superstrate layer is $\lambda/6$.

As the separation distance between the RMPA and the MTM slab increased from 10mm to 60mm, a considerable improvement in gain and fluctuation in reflection coefficient has been observed. When the separation distance is 50mm, a reflection coefficient of −21.82dB, a bandwidth (BW) of 34.50MHz (1.0785GHz – 1.0440GHz), and a gain of 7.4dB has been recorded at 1.06GHz resonating frequency. In comparison to the proposed RMPA, which has a reflection coefficient of −19.52dB, a BW of 13.10MHz (1.0740GHz – 1.0609GHz), and a gain of 4.6dB, the deployment of an NRI MTM slab with 5 × 4 SCM unit-cell on the RMPA has improved the gain and BW of the antenna up to 2.8dB, and 21.40MHz, respectively.

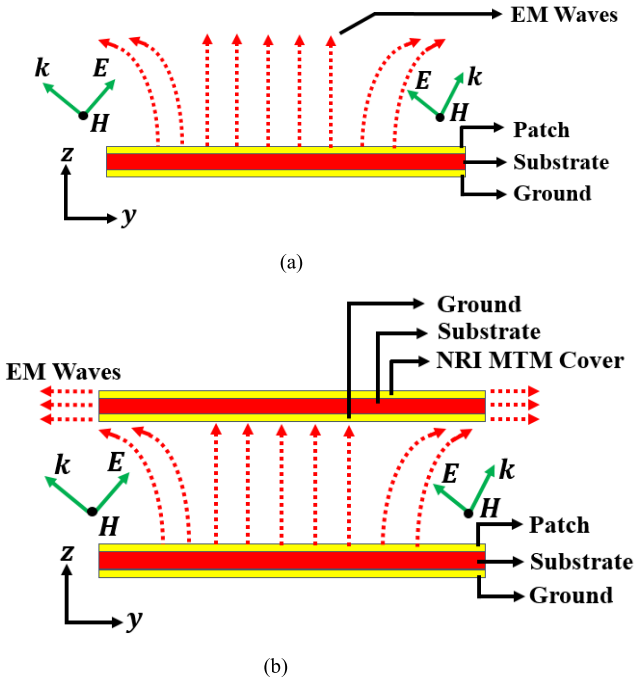

FIGURE 28. Gain enhancement mechanism (a) without NRI-MTM cover and (b) with NRI-MTM cover.

The role of the NRI MTM slab on the field distribution and antenna gain improvement can be analyzed with the aid of Figure 28. In the proposed RMPA, as depicted in Figure 28 (a), the propagation of EM waves along the sides is perpendicular to the YOX plane. The use of MTM as a superstrate will distract EM wave propagation, and the NRI properties of MTM will divert the flow of EM waves in the horizontal direction, as depicted in Figure 28 (b). As a result, the proposed NRI MTM slab as a superstrate increases the density of EM wave propagation in the horizontal direction parallel to the YOX plane. The increase in horizontal wave propagation caused by the MTM slab modifies the primary beam direction, enhancing the horizontal gain [39].

TABLE 8 compares the proposed NRI-MTM previous work in terms of MTM shape and type, number of resonant bands, gain improvement approaches, EMR, and applications.

TABLE 8. Optimal dimensions of the proposed RMPA.

Ref	Year	Electrical dimension (mm^2)	Resonating Frequency (GHz)	No. of Resonance	MTM shape	MTM type	Gain Enhancement Technique	Gain Enhancement (dB)	EMR	Application
[46]	2014	12.3×12.3	1.8	1	Square SRR	NRI	Superstrate	1.91	13.5	RF energy harvesting
[47]	2015	11.15×11.4	2.4	1	Square CSRR	NRI	MTM loaded ground	1.13	10.9	S-Band applications
[48]	2016	30×30	2.4	1	Square	Near-zero refractive index (NZRI)	Superstrate	2.3	4.1	WLAN
[49]	2016	27.5×27.5	0.95	1	Triangle-shape	NRI	Superstrate	2.32	11.5	RF energy harvesting
[50]	2017	24.9×24.9	0.95	1	Nested Square	NRI	Superstrate	2.64	12.2	RF energy harvesting
[51]	2018	35×35	2.4	1	Phi-Shaped SRR	NRI	Superstrate	2.71	4.2	S-Band Application
[52]	2018	26.25 ×24.15	2.6	1	Square ring with diagonal strip	Epsilon-and-Mu-Near-Zero (EMNZ)	Superstrate	3.5	4.39	S-Band Application
[53]	2020	15×15	2.45	1	Ω-shape	μ very large (MVL)	MTM loaded ground	2.58	8.2	Biomedical
[54]	2021	22.5 × 22.5	2.4	1	G-shape	NZRI	Superstrate	4	5.5	WLAN
Proposed	**2022**	**23×23**	**1.06**	**1**	**Coupled square and circle**	**NRI**	**Superstrate**	**2.8**	**12.6**	**Aircraft surveillance**

V. CONCLUSION AND FUTURE SCOPE

In this research, the combination of square and circular split ring structure is proposed for TCAS application. The effective parameters such as permittivity, permeability, and refractive index of this SCM structure are computed using MATLAB. Initially, a single SCM unit-cell is designed and its effective parameters are computed. The computation of the above parameters predicts that, this SCM unit-cell is behaving as a DNG material over the frequency range of 0.5 - 1.2 GHz. The DNG SCM unit-cell is then extended to 5 × 4 array and is utilized as a superstrate over a designed rectangular patch antenna to enhance the gain. It was observed that, the loading of superstrate layer has enhanced the gain from 4.6 dB to 7.4 dB, and bandwidth from 13.10 MHz to 34.5 MHz. Thus, the proposed NRI-MTM is well-suited for surveillance application. A detailed parametric analysis of the unit-cell and array is performed to fix the dimension, spacing between rings, spacing between unit-cells, width of each ring, and split width to prove the efficacy of the designed MTM structure.

In aircraft surveillance applications, an antenna with a high gain and a wider bandwidth is required to broadcast and receive a highly directional signal in a specific direction, as well as to cover a larger surveillance zone and enhance airspace efficiency. Thus, future development for the aforementioned application includes the use of the proposed SCM array to improve the gain of MIMO antenna. In addition, the designed SCM unit-cell structure can be used as a decoupling structure to improve the isolation of the MIMO antenna for TCAS application. The pattern and polarization reconfigurability might also be planned by deploying PIN diode switches at the relevant split gaps of the designed SCM unit-cell.

REFERENCES

[1] R. Liu, C. Ji, Z. Zhao, and T. Zhou, "Metamaterials: Reshape and rethink," *Engineering*, vol. 1, no. 2, pp. 179–184, 2015.
[2] Z. Ni, "Metamaterials at the University of Southampton metamaterials at the University of Southampton and beyond," *J. Opt.*, vol. 19, no. 8, pp. 1–18, 2017.
[3] M. Pallavi, P. Kumar, T. Ali, and S. B. Shenoy, "A review on gain enhancement techniques for vertically polarized mid-air collision avoidance antenna for airborne applications," *IEEE Access*, vol. 9, pp. 30761–30792, 2021.
[4] M. Lashab, C. Zebiri, F. Benabdelaziz, N. A. Jan, and R. Abd-Alhameed, "Horn antennas loaded with metamaterial for Ku band application," in *Proc. Int. Conf. Multimedia Comput. Syst. (ICMCS)*, 2014, vol. 1327, no. 1375, pp. 14–16.
[5] T. Ramachandran, F. Mri, and E. Ahamed, "Composite circular split ring resonator (CSRR)-based left-handed metamaterial for C- and Ku-band application," *Results Phys.*, vol. 14, Sep. 2019, Art. no. 102435.
[6] F. Mri and H. Mi, "Effects of hand on EM absorption and antenna performances for internal handset PIFA," in *Proc. Vjesn*, vol. 24, 2017, pp. 459–467.
[7] Y. J. Yoo, S. Ju, S. Y. Park, Y. J. Kim, J. Bong, T. Lim, K. W. Kim, J. Y. Rhee, and Y. Lee, "Metamaterial absorber for electromagnetic waves in periodic water droplets," *Sci. Reports*, vol. 5, pp. 3–10, Sep. 2015.
[8] L. Basudev, "Split Ring Resonator (SRR) based metamaterials," M.S. thesis, Univ. Glasgow, Glasgow, U.K., 2010. [Online]. Available: https://eleanor.lib.gla.ac.uk/record=b2774207
[9] R. W. Ziolkowski and E. Nader, *Introduction, History, and Selected Topics in Fundamental Theories of Metamaterials*, E. Nader and R. W. Ziolkowski, Eds. Hoboken, NJ, USA: Wiley, 2006, pp. 1–41.
[10] M. J. Alam, M. R. I. Faruque, T. Allen, S. Abdullah, and M. T. Islam, "Depiction and analysis of a modified theta shaped double negative metamaterial for satellite application," *Open Phys.*, vol. 16, no. 1, pp. 839–847, 2018.
[11] N. I. Zheludev, "The road ahead for metamaterials," *Appl. Phys.*, vol. 382, no. 5978, pp. 582–583, 2010.

[12] T. Ramachandran, F. Mri, E. Ahamed, and S. Abdullah, "Specific absorption rate reduction of multi split square ring metamaterial for L- and S-band application," *Results Phys.*, vol. 15, pp. 1–10, Dec. 2019.

[13] R. Maas, J. Parsons, N. Engheta, and A. Polman, "Experimental realization of an epsilon near-zero metamaterial at visible wavelengths," *Nature Photon.*, vol. 7, pp. 907–912, Sep. 2013.

[14] H. Singh, N. Mittal, and O. Arora, "Designing and analysis of frequency reconfigurable double negative flower leaf metamaterial resonator," *Mater. Today, Proc.*, vol. 33, no. 3, pp. 1552–1557, 2020.

[15] N. Engheta, A. Alu, R. W. Ziolkowski, and A. Erentok, "Fundamentals of waveguide and antenna applications involving DNG and SNG metamaterials," in *Metamaterials: Physics and Engineering Explorations*, N. Engheta and R. W. Ziolkowski Eds. Piscataway, NJ, USA: Institute of Electrical and Electronics Engineers, 2006, pp. 43–85.

[16] H. Singh, B. S. Sohi, and A. Gupta, "A compact CRLH metamaterial with wide band negative index characteristics," *Bull. Mater. Sci.*, vol. 42, pp. 1–11, Jun. 2019, doi: 10.1088/2053-1591/AB1196.

[17] N. Wongkasem, A. Akyurtlu, and K. Marx, "Group theory based design of isotropic negative refractive index metamaterials," *Prog. Electromagn. Res.*, vol. 63, pp. 295–310, 2006.

[18] V. G. Veselago, "The electrodynamics of substances with simultaneously negative values of ε and μ," *Sov. Phys.*, vol. 10, no. 4, pp. 509–514, Jan. 1968.

[19] J. B. Pendry, A. J. Holden, W. J. Stewart, and I. Youngs "Extremely low frequency plasmons in metallic mesostructures," *Phys. Rev. Lett.*, vol. 76, no. 25, p. 4773, 1996.

[20] J. B. Pendry, A. J. Holden, D. J. Robbins, and W. J. Stewart, "Magnetism from conductors and enhanced nonlinear phenomena," *IEEE Trans. Microw. Theory Techn.*, vol. 47, no. 11, pp. 2075–2084, Nov. 1999.

[21] D. R. Smith, W. J. Padilla, D. C. Vier, S. C. Nemat-Nasser, and S. Schultz, "Composite medium with simultaneously negative permeability and permittivity," *Phys. Rev. Lett.*, vol. 84, no. 18, p. 4184, 2000.

[22] R. A. Shelby, D. R. Smith, and S. Schultz, "Experimental verification of a negative index of refraction," *Science*, vol. 292, no. 5514, pp. 77–79, Apr. 2001.

[23] S. S. Islam, M. A. Rahman, M. R. I. Faruque, and M. T. Islam, "Design and analysis with different substrate materials of a new metamaterial for satellite applications," *Sci. Eng. Composite Mater.*, vol. 25, no. 1, pp. 59–66, 2018.

[24] H. A. Majid, M. K. A. Rahim, and T. Masri, "Microstrip antenna's gain enhancement using left-handed metamaterial structure," *Prog. Electromagn. Res. M*, vol. 8, pp. 235–247, 2009.

[25] C. Sabah, "Tunable metamaterial design composed of triangular split ring resonator and wire strip for S- and C-microwave bands," *Prog. Electromagn. Res. B*, vol. 22, pp. 341–357, 2010.

[26] S. Li, A. Z. Elsherbeni, W. Yu, W. Li, and Y. Mao, "A novel tunable triple-band left-handed metamaterial," *Int. J. Antennas Propag.*, vol. 2017, Dec. 2017, Art. no. 7583736.

[27] O. Yurduseven, A. E. Yilmaz, and G. Turhan-Sayan, "Hybrid-shaped single-loop resonator: A four-band metamaterial structure," *Electron. Lett.*, vol. 47, no. 25, pp. 1381–1382, Dec. 2011.

[28] S. Xi, H. Chen, B. I. Wu, and J. Kong, "Experimental confirmation of guidance properties using planar anisotropic left-handed metamaterial slabs based on S-ring resonators," *Prog. Electromagn. Res.*, vol. 84, pp. 279–287, 2008.

[29] L. X. Ran, J. T. Huang-Fu, H. Chen, X. M. Zhang, K. Chen, T. M. Grzegorczyk, and J. Kong, "Experimental study on several left-handed matamaterials," *Prog. Electromagn. Res.*, vol. 51, pp. 249–279, 2005.

[30] J. Wang, S. Qu, J. Zhang, H. Ma, Y. Yang, C. Gu, X. Wu, and Z. Xu, "A tunable left-handed metamaterial based on modified broadside-coupled split-ring resonators," *Prog. Electromagn. Res. Lett.*, vol. 6, pp. 35–45, 2009.

[31] M. J. Alam, E. Ahamed, M. R. I. Faruque, M. T. Islam, and A. M. Tamim, "Left-handed metamaterial bandpass filter for GPS, Earth Exploration-Satellite and WiMAX frequency sensing applications," *PloS One*, vol. 14, no. 11, 2019, Art. no. e0224478.

[32] S. S. Islam, M. S. Khan, and M. R. I. Faruque, "Design and analysis of modified-split-H-shaped DNG metamaterial for microwave application," *Mater. Res. Exp.*, vol. 6, no. 12, 2020, Art. no. 125808.

[33] D. De and P. K. Sahu, "Design and development of a multi-feed end-fired microstrip antenna for TCAS airborne system," *Prog. Electromagn. Res. C*, vol. 78, pp. 69–81, 2017.

[34] A. Vallecchi, E. Shamonina, and C. J. Stevens, "Analytical model of the fundamental mode of 3D square split ring resonators," *J. Appl. Phys.*, vol. 125, no. 1, 2019, Art. no. 014901.

[35] O. Sydoruk, E. Tatartschuk, E. Shamonina, and L. Solymar, "Analytical formulation for the resonant frequency of split rings," *J. Appl. Phys.*, vol. 105, no. 1, 2009, Art. no. 014903.

[36] M. R. Islam, M. T. Islam, M. Moniruzzaman, M. Samsuzzaman, B. Bais, H. Arshad, and G. Muhammad, "Square enclosed circle split ring resonator enabled epsilon negative (ENG) near zero index (NZI) metamaterial for gain enhancement of multiband satellite and radar antenna applications," *Results Phys.*, vol. 19, Aug. 2020, Art. no. 103556.

[37] X. Chen, T. M. Grzegorczyk, B.-I. Wu, J. Pacheco, Jr., and J. A. Kong, "Robust method to retrieve the constitutive effective parameters of metamaterials," *Phys. Rev. E, Stat. Phys. Plasmas Fluids Relat. Interdiscip. Top.*, vol. 70, no. 1, 2004, Art. no. 016608.

[38] K. Li, S. J. McLean, R. B. Greegor, C. G. Parazzoli, and M. H. Tanielian, "Free-space focused-beam characterization of left-handed materials," *Appl. Phys. Lett.*, vol. 82, no. 15, pp. 2535–2537, 2003.

[39] M. Moniruzzaman, M. T. Islam, N. Misran, M. Samsuzzaman, T. Alam, and M. E. Chowdhury, "Inductively tuned modified split ring resonator based quad band epsilon negative (ENG) with near zero index (NZI) metamaterial for multiband antenna performance enhancement," *Sci. Rep.*, vol. 11, no. 1, pp. 1–29, 2021.

[40] A. M. Siddiky, M. R. I. Faruque, M. T. Islam, and S. Abdullah, "A multi-split based square split ring resonator for multiband satellite applications with high effective medium ratio," *Results Phys.*, 22, Mar. 2021, Art. no. 103865.

[41] M. M. Bait-Suwailam, *Electromagnetic Fields and Waves*. London, U.K.: IntechOpen, 2019.

[42] M. R. Akram, C. He, and W. Zhu, "Bi-layer metasurface based on Huygens' principle for high gain antenna applications," *Opt. Exp.*, vol. 28, no. 11, pp. 15844–15854, 2020.

[43] N. Mishra, D. K. Choudhary, R. Chowdhury, K. Kumari, and R. K. Chaudhary, "An investigation on compact ultra-thin triple band polarization independent metamaterial absorber for microwave frequency applications," *IEEE Access*, vol. 5, pp. 4370–4376, 2017.

[44] G. Von Trentini, "Partially reflecting sheet arrays," *IRE Trans. Antennas Propag.*, vol. 4, no. 4, pp. 666–671, Oct. 1956.

[45] H. Liu, S. Lei, X. Shi, and L. Li, "Study of antenna superstrates using metamaterials for directivity enhancement based on Fabry–Pérot resonant cavity," *Int. J. Antennas Propag.*, vol. 2013, Feb. 2013, Art. no. 209741.

[46] K. K. A. Devi, N. C. Hau, C. K. Chakrabarty, and N. M. Din, "Enhancement of band width and gain by using 3×4 array of metamaterial based patch antenna for RF energy harvesting at GSM 1800," *Int. J. Eng. Res.*, vol. 3, no. 10, pp. 618–623, 2014.

[47] R. Pandeeswari and S. Raghavan, "Microstrip antenna with complementary split ring resonator loaded ground plane for gain enhancement," *Microw. Opt. Technol. Lett.*, vol. 57, no. 2, pp. 292–296, 2015.

[48] J. Li, T. A. Denidni, and Q. Zeng, "A compact gain-enhancement patch antenna based on near-zero-index metamaterial superstrate," in *Proc. 17th Int. Symp. Antenna Technol. Appl. Electromagn. (ANTEM)*, Jun. 2016, pp. 1–2.

[49] K. A. Devi, N. C. Hau, C. Chakrabarty, and N. M. Din, "A negative refractive index metamaterial structure for antenna gain enhancement," *Int. J. Eng. Works*, vol. 2, no. 12, pp. 93–98, 2016, doi: 10.5281/zenodo.49361.

[50] C. H. Ng, K. K. A. Devi, C. K. Chakrabarty, N. Din, and C. F. Kwong, "Gain enhancement of microstrip patch antenna using low loss negative refractive index metamaterial superstrate," *J. Telecommun. Electron. Comput. Eng. Summ.*, vol. 9, no. 1, pp. 95–99, 2013.

[51] M. Saravanan and S. M. Umarani, "Gain enhancement of patch antenna integrated with metamaterial inspired superstrate," *J. Electr. Syst. Inf. Technol.*, vol. 5, no. 3, pp. 263–270, 2018.

[52] P. K. Panda and D. Ghosh, "Isolation and gain enhancement of patch antennas using EMNZ superstrate," *AEU-Int. J. Electron. Commun.*, vol. 86, pp. 164–170, Mar. 2018.

[53] G. K. Das, S. Basu, B. Mandal, D. Mitra, R. Augustine, and M. Mitra, "Gain-enhancement technique for wearable patch antenna using grounded metamaterial," *IET Microw., Antennas Propag.*, vol. 14, no. 15, pp. 2045–2052, 2020.

[54] B. K. A. Shaji, A. Pradeep, and P. Mohanan, "Fractal inspired metamaterial superstrate for gain enhancement," *Int. J. Commun. Antenna Propag.*, vol. 11, no. 4, pp. 271–278, 2021.

M. PALLAVI (Member, IEEE) received the B.E. degree in instrumentation technology and the M.Tech. degree in information and communication systems from Visvesvaraya Technological University, Belgaum, India, in 2009 and 2011, respectively. She is currently pursuing the Ph.D. degree with the Department of Electronics and Communication Engineering, Manipal Institute of Technology, Manipal Academy of Higher Education, Manipal, India.

Her current research interests include feeding mechanism for antenna, linearly polarized microstrip antennas, microstrip antenna applications, and performance enhancement techniques for microstrip antennas. She is an Associate Member of IETE and ISTE.

PRAMOD KUMAR (Senior Member, IEEE) received the B.E. degree in electronics and communication engineering from Visvesvaraya Technological University, in 2002, the M.Tech. degree in microwave engineering from the Madhav Institute of Technology and Science, Gwalior, India, in 2007, and the Ph.D. degree from the Department of Electrical and Electronics Engineering, National Institute of Technology Karnataka, Mangaluru, India. He is currently a Professor with the Department of Electronics and Communication Engineering, Manipal Institute of Technology, Manipal, India. He is guiding four research scholars in the area of antennas engineering and the IoT-based wireless sensor networks. He has published more than 50 papers in reputed peer-reviewed international journals and conferences. His current research interests include the IoT-based wireless sensor networks, antennas engineering, and measurement of heart rate variability of ECG signal. He is a Faculty Advisor of the IEEE ComSoc Student Chapter MIT Manipal. He is on the Board of Reviewers of journals, such as the IEEE TRANSACTIONS ON ANTENNAS AND PROPAGATION, *IET Networks*, the *AEU-International Journal of Electronics and Communications*, *Wireless Personal Communications* (WPC), the *International Journal of Microwave and Wireless Technologies*, the *International Journal of Communication*, and *Telecommunication systems*. He also serves as an editor and chaired of many international conferences, such as ICCWC-2022 (www.iccwc.in) and AICECS 2021 (http://www.aicecs.com).

TANWEER ALI (Senior Member, IEEE) is currently an Assistant Professor-Senior Scale with the Department of Electronics and Communication Engineering, Manipal Institute of Technology, Manipal Academy of Higher Education, Manipal. He is also an Active Researcher in the field of microstrip antennas, wireless communication, and microwave imaging. He is also guiding four regular Ph.D. students and five part-time Ph.D. students, and is heading the Antenna Research Group, MIT, Manipal. He has been listed in the Top 2% Researcher across the world recently by the prestigious list published by Stanford University, USA, indexed by Scopus. He has published more than 115 papers in reputed web of science (SCI) and Scopus indexed journal and conferences, and also has filled two Indian patents. He has more than 1000 citations with an H-index of 19 and i10-index of 28. In 2020, he has received the Best Ph.D. Thesis Award from the Board of IT Education (BITES), Karnataka. He is on the Board of Reviewers of journals, such as the IEEE TRANSACTIONS ON ANTENNAS AND PROPAGATION, IEEE ANTENNAS AND WIRELESS PROPAGATION LETTERS, IEEE ACCESS, *IET Microwaves, Antennas and Propagation*, *Electronics Letters* (IET), *Wireless Personal Communications* (WPCs) (Springer), *AEU-International Journal of Electronics and Communications*, *Microwave and Optical Technology Letters* (MOTL) (Wiley), the *International Journal of Antennas and Propagation* (Hindawi), *Advanced Electromagnetics*, *Progress in Electromagnetics Research* (PIER), *KSII Transactions on Engineering Science*, the *International Journal of Microwave and Wireless Technologies*, *Frequenz*, *Radioengineering*, and IEEE OPEN JOURNAL OF ANTENNAS AND PROPAGATION.

SATISH B. SHENOY (Member, IEEE) is currently a Professor with the Department of Aeronautical and Automobile Engineering, Manipal Institute of Technology (MIT), Manipal Academy of Higher Education, Manipal. He is on the Mentor Board of the Center for Excellence in Avionics and Navigation Systems, MIT. He is also an Active Researcher in the field CFD, FEM, and CAD. He has published more than 105 articles in reputed peer-reviewed journals. He is a Life Member of TSI. He is on the Board of Reviewers of journals, such as *Tribology International*, *Proceedings of the Institution of Mechanical Engineers—J: Journal of Engineering Tribology*, *Computer Methods in Biomechanics and Biomedical Engineering*, *Journal of the Brazilian Society of Mechanical Sciences and Engineering*, *Simulation Modelling Practice and Theory*, *Tribology Transactions*, *Industrial Lubrication and Tribology*, *Journal of Tribology*, *Polymer Testing*, *Acta Radiologica*, *Journal of Bionic Engineering*, *Journal of Marine Science and Application*, *Mechanics & Industry*, and *Polymer Composites*.